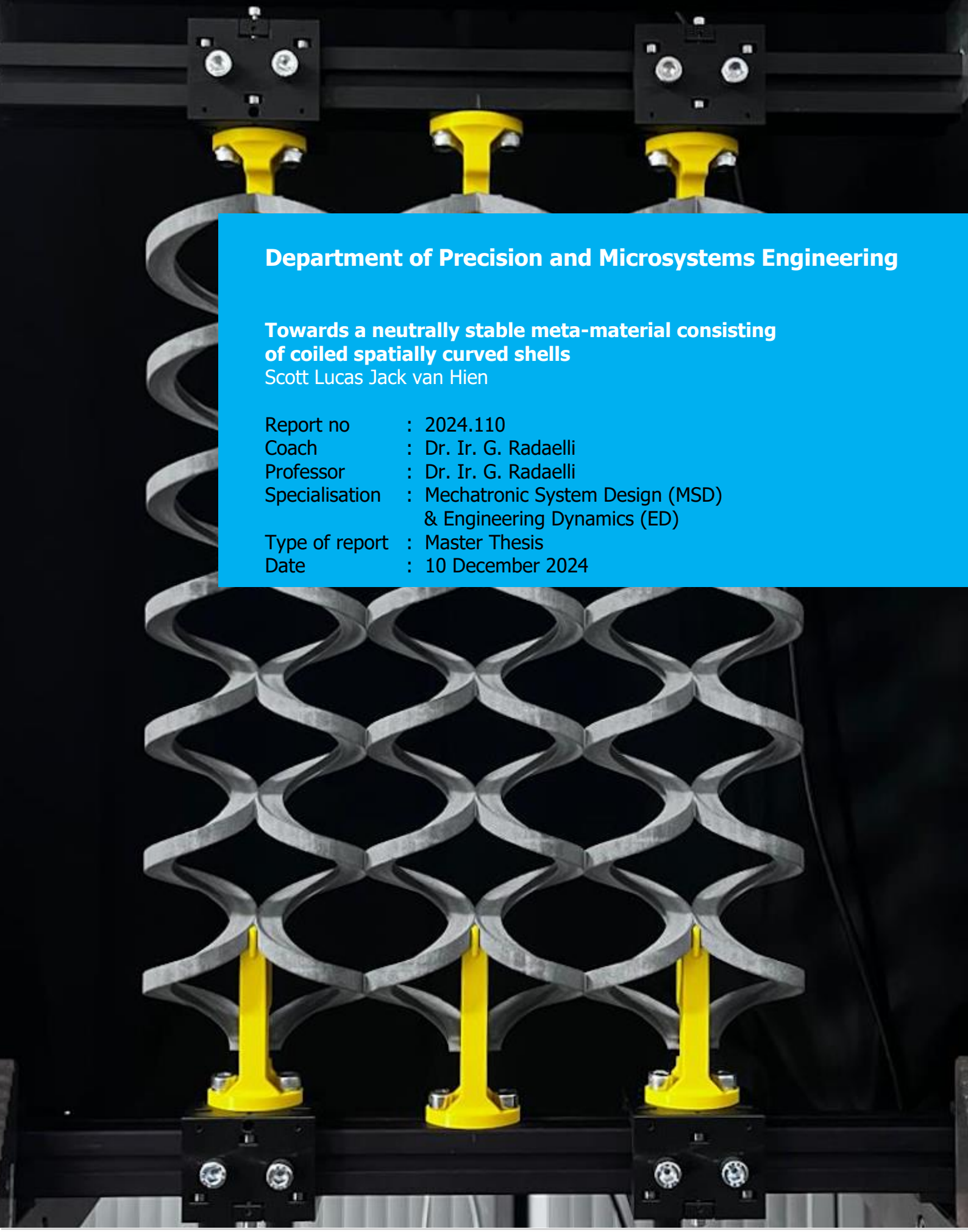

Department of Precision and Microsystems Engineering

Towards a neutrally stable meta-material consisting of coiled spatially curved shells

Scott Lucas Jack van Hien

Report no	:	2024.110
Coach	:	Dr. Ir. G. Radaelli
Professor	:	Dr. Ir. G. Radaelli
Specialisation	:	Mechatronic System Design (MSD) & Engineering Dynamics (ED)
Type of report	:	Master Thesis
Date	:	10 December 2024

TU Delft Delft University of Technology

Challenge the future

Delft University of Technology

Department of Precision and Microsystem Engineering

Towards a neutrally stable meta-material consisting of coiled spatially curved shells

Design, evaluation, and optimization of a coiled spatially curved shell structure exhibiting zero-stiffness behaviour during compression to facilitate neutrally stable behaviour in a meta-material.

By:

Scott Lucas Jack van Hien

Student number:	5128056	
Project duration:	September 1st, 2023 – December 20th, 2024	
Thesis committee:	Dr. ir. G. Radaelli,	TU Delft, chair
		TU Delft, daily supervisor
	D. Farhadi Machekposhti,	TU Delft, committee member

Tuesday 10th December, 2024

Keywords: constant force, meta-material, neutral stability, shell, spatially curved, zero-stiffness

Abstract

Meta-materials provide many possibilities with their specially tailored properties on the macro level caused by their micro level structure in the form of unit cells. These unit cells often take the form of Compliant Mechanisms (CM), which have been widely researched. CM are often made neutrally stable to improve their energy efficiency, making it plausible that meta-materials can be made neutrally stable as well. This research aims to create such a neutrally stable meta-material using constant force (zero-stiffness) unit cells. This was achieved by optimizing the geometry of coiled spatially curved shell structures such that their buckling mode under compression facilitated a constant force region under compression. Simulations of the optimized structures within a meta-material lattice are compared to experimental tests performed on 2 different prototypes of such a meta-material. The experimental results show that the force-displacement curves indeed have a constant force trend line under compression. However, the magnitude of the trend line for one experiment is significantly lower than expected in the simulations. Despite this magnitude difference, the shapes of the experimental force-displacement curves are similar to the curves of the simulations. Small regions of neutral stability are observed for the deformed unit cells of the meta-material, but sawtooth-like behaviour of the force-displacement curves around the trend line caused these regions to be small and unstable.

Contents

1 Introduction

A relatively new and promising field in engineering is that of meta-materials. A meta-material is a lattice comprised of several unit cells that exhibit characteristics that do not exist in conventional engineering materials. Optical[1], acoustical[2], and mechanical[2] behaviours can be tuned by changing the properties of the unit cell on the micro level. This causes the meta-material as a whole to gain certain properties at the macro level[2]. For example, unit cells could manipulate light in such a way that the meta-material as a whole has a negative refractive index[1]. Or, the deformation of unit cells is such that the meta-material shrinks in width when it is compressed instead of expanding (negative Poisson ratio)[2]. Additionally, a meta-material is scalable as long as the production method allows for smaller unit cells and/or larger lattices. Therefore, these innovative materials could provide a wide range of possibilities in the industry for specialized applications.

The unit cells of meta-materials are often specialized Compliant Mechanisms (CM). CM function by the deformation of slender elastic segments and are often monolithic, which eliminates friction between components. This facilitates low wear, low particle generation, high precision, and scalability[3]. CM do suffer in energy efficiency, as the input energy of a CM is partially stored as strain energy[4]. To combat this, CM are made neutrally stable: for a certain Range of Motion (RoM) the mechanism has no changes in its potential energy. In other words, the CM would not generate elastic restoring forces that attempt to revert it back to another neutral state[5]. This makes the neutrally stable CM energy efficient, as minimal effort is required during actuation.

To achieve neutral stability in a CM it has to be prestressed: introducing an energy buffer that adds negative stiffness to balance the elastic forces from deformation[5]. There are several prestressing methods for this such as thermal treatments, introducing plastic deformations, and curing a polymer matrix with fibers embedded within the material. The latter method introduces the prestress as a result of the different shrink rates of the polymer and the embedded fibers[6]. An example of a neutrally stable CM that used plastic deformation as its prestressing method was created by *Guest et al*[7]. The shell had been cold-rolled about two perpendicular axis, facilitating the neutrally stable behaviour. As seen in Figure 1.1, the shell remains in its current orientation without the need for external forces.

Figure 1.1: Neutrally stable shell[5]

Keeping this in mind, it seems plausible that meta-materials can be made neutrally stable - since these are often comprised of several CM. However, in literature the closest example found are near zero-stiffness meta-materials[8]. The difference here is that with neutral stability constant force (zero-stiffness) at a zero-force level is achieved, keeping the potential energy constant. The absence of neutrally stable meta-materials in the literature could be explained by the complex process of applying prestress to them. To prestress a meta-material each of its individual unit cells should be prestressed identically, such that the behaviour of the meta-material stays consistent and behaves as expected. This quickly restricts the usage of plastic deformation and fiber curing methods, as complex spatial orientations can be cumbersome to shape identically for all unit cells. Thermal treatments are still an option but are limited to the size and material of the meta-material, while also having lower chances of consistent results throughout the entire lattice.

If there is a way to prestress the meta-material via a uniform and simple method, it could make meta-materials more versatile. Looking in the literature, spatial shell structures quickly emerge with interesting prospects. In an example from *Radaelli et al.*, a spatially curved shell structure was designed that has neutral stability under a certain gravitational force[9]. In another example from *Kok et al.*, neutrally stable behaviour is attained with two compliant shells connected by a curved crease.[10]. Here, the potential energy was minimized by tailoring the transition region around the inflection point such that the structure could transition smoothly between equilibrium configurations with minimal effort. Instead of relying on complex prestressing strategies, these papers utilize part of the deformation range in the intended Degree of Freedom (DoF) as the prestressing action. This is achieved by optimizing the geometry of the shell structures, such that the force response in the intended DoF facilitates enough prestress during deformation. While deforming the shell its elastic forces balance each other out, ensuring a constant energy potential. This raises the question whether it is possible to create a meta-material in which the geometry of the unit cell is designed in such a way that it can provide neutral stability under certain loading conditions.

Considering a meta-material constructed of spatially curved shell structures, the constraints that the meta-material lattice imposes on the individual unit cells can potentially be exploited. In literature it is suggested that neutral stability can be achieved using constant force (zero-stiffness) springs, which oppose each other's forces[11]. If the unit cell's geometry can be tuned in such a way to attain a constant force profile, the meta-material as a whole would then have regions of neutral stability embedded within. To achieve constant force in a spatially curved shell, intentional buckling can prove to be a viable method[5]. Coiled spatially curved shell structures are suitable candidates for this, as they can buckle in compression and elongation depending on their geometry. Additionally, these shell structures have a lower stiffness in this deformation DoF compared to its other translational Dofs. This could result in a meta-material that is prestressed via compression/elongation, making the meta-material relatively easy to prestress compared to the aforementioned methods. When deformed to a certain threshold, each unit cell would be in its constant force region. This ensures each unit cell would balance out its neighbours under deformation, resulting in a neutrally stable meta-material.

1.1. Research goal

It is hypothesized that a desirable stiffness behaviour can be tailored for a coiled spatially curved shell structure by changing its geometry. This would yield a simple prestressing method resulting in a neutrally stable meta-material. The research goal of this paper is therefore to:

To design and optimize the geometry of a coiled spatially curved shell structure in such a way that - when embedded in a meta-material lattice - they function as constant force (zero-stiffness) spring. Neutral stability is then to be achieved by opposing the unit cells constant force-displacement profiles.

1.2. Thesis outline

This report begins with the design process followed in chapter 2. The results from the simulations and experiments are elaborated upon in chapter 3. In chapter 4 the assumptions made in the methodology and the results are discussed. The conclusions of this paper are summarized in chapter 5.

2 Methodology

This chapter details the methodology that is followed throughout this research. First, the basic geometry of the coiled spatially curved shell structure and its placement within the meta-material lattice will be detailed in section 2.1. Second, the numerical model used to optimize the geometry of this structure is explained in section 2.2. Lastly, the fabrication method and test setup for the prototypes to validate the optimization simulation are explained in section 2.3.

2.1. Geometry

The design process of this research considers geometry optimization of a coiled spatially curved shell - now to be called *structure* - that consists of a U cross-section drawn along a helix profile, as seen in Figure 2.1. Buckling of the structure is to be used as this could facilitate a constant force (zero-stiffness) response of the unit cell[5]. There are a few reasons why the depicted geometry was chosen. First, the helix profile is chosen as it provides a lower stiffness in the actuation translational DoF already, while keeping the other translational DoF and the torsional DoF stiffnesses relatively high. The stiffnesses of the bending DoF remain relatively similar to those of the actuation DoF. However, since this structure is to be placed in a lattice, it is hypothesized these stiffnesses will become relatively high because of those extra constraints. Second, the U cross-section is chosen because the middle/back-flange - now to be called *spine* - can be flat. This is beneficial as it simplifies the connection points within the meta-material lattice as lines, while also providing simple interfaces for testing setups. Lastly, the side flanges - now to be called *flanges* - can be loaded in compression (resulting in buckling), regardless whether the meta-material is loaded in compression or tension. If the flanges point inwards, the meta-material can be loaded in compression. If they point outwards, the meta-material can be loaded in tension. Hypothetically speaking, both could be achieved by pointing the flanges to both sides. For this research the flanges point inwards as this provides the most straightforward lattice configuration (spines fused back to back) for fabrication, as seen in Figure 2.2 and Figure 2.3). Since the spine remains flat, changing the flange geometry is the main contributor to the stiffness behaviour when the structure is deformed.

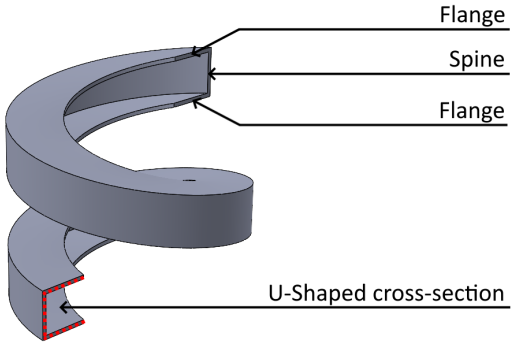

Figure 2.1: Structure with U-shaped cross-section drawn along a helix profile

The structure's geometry is defined by several parameters which can be optimized. Running optimizations with too many variables requires significant computational time, which should be avoided. Additionally, it is unclear what parameters affect the structure's performance the most. Therefore, a parameter sensitivity analysis was conducted (see Appendix B) such that adequate parameters could be selected for optimization. Here, it was concluded that it is most efficient to optimize for the following 6 variables: flange *shape* - consisting of 5 X-coordinates - and *ratio*. The shape entails how the flanges are formed. For example, in Figure 2.1 the flange shape is a straight line. The ratio describes the length of the flanges (l) with respect to the length of the spine (L).

As mentioned before, the spines of each structure are to be merged where they touch the spine of the other individual structures. This can produce two types of meta-material lattices: *planar* and *spatial*. The planar lattice will have structures next to each other, meaning that an individual structure's spine has "neighbours" in just 1 dimension, as seen in Figure 2.2. The unit cell of the meta-material is therefore defined as two mirrored structures back-to-back for the planar lattice, indicated with a brown rectangle in the figure. For the spatial lattice an individual structure's spine will have "neighbours" in 2 dimensions, as seen in Figure 2.3. The unit cell of the meta-material is therefore defined as two mirrored planar unit cells back-to-back for the spatial lattice, indicated with a purple rectangle in the figure. Furthermore, the planar lattice type has constraints on each spine at every half revolution, and the spatial lattice type has constraints on each spine at every quarter revolution. This means the lattice type will influence the stiffness characteristics of the structure.

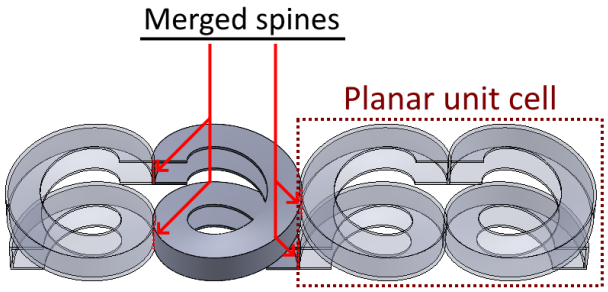

Figure 2.2: Merged spines on a planar lattice

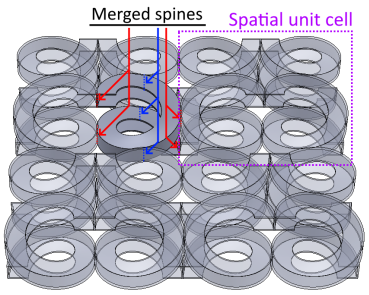

Figure 2.3: Merged spines on a spatial lattice

2.2. Optimization

This section details the optimization process that is used to create the optimal geometry for the desired constant force (zero-stiffness) structure. In subsection 2.2.1 the numerical model of the structure is elaborated on. This is followed by the setup of the optimization runs in subsection 2.2.2.

2.2.1. Numerical model

It is assumed all structures deform uniformly. Therefore, the model consists of a one-revolution version of the structure. Depending on the lattice type, it has constraints to simulate as if it is positioned in a meta-material lattice. Here, the meta-material is infinitely long in 2 directions for the planar lattice simulations and infinitely long in all directions for the spatial lattice simulations. The structure is modeled by an isotropic and linear material model using a Kirchoff-Love class continuum, which is able to undergo large deformations. The thickness is considered uniform for the entire mesh. The FEA model used to solve this mesh is based on Isogeometric analysis[12]. The model was then constructed as follows: First, the cross-section shape is defined by a Non-Uniform Rational Basis Spline - or NURBS for short - that uses certain parameter inputs. In Figure 2.4 the NURBS are depicted for the entire cross-section. Here, the NURBS nodes depicted with an **X** indicate the nodes that require a parameter input. The NURBS nodes depicted with an **O** indicate the fixed nodes. The variable nodes (Blue) therefore model the flanges and the fixed nodes (Red) model the spine of the structure. Second, the cross-section is meshed along a helix defined by the other parameters to construct the mesh of the entire structure. The mesh parameters are [n x m]. Here, n models the nodes on the cross-section itself and m models the amount of cross-sections drawn along the helix. For the simulations these mesh parameters were set to [21 x 51]. Note that n and m both must be odd numbers for proper placement of constraints.

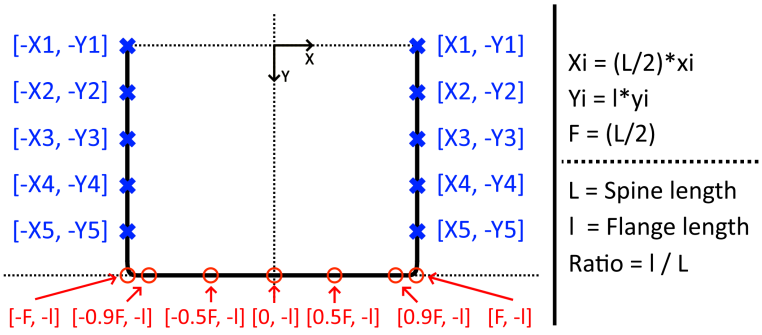

Figure 2.4: NURBS nodes that define the cross-section

Before this mesh can be solved, periodic boundary conditions are needed that simulate the meta-material in which the structure is embedded. First, the merged spines should be simulated. As mentioned in chapter 2, these are simplified as line connections. These lines should follow a few conditions to make them behave as if in the meta-material lattice:

- The line should be free to translate only in the desired plane tangent to the spine.
- The line should not be able to rotate about the axis perpendicular to the tangent plane.
- A line constraint should always be collinear with line constraints that are exactly an integer of a revolution further/earlier on the structure if applicable.

In Figure 2.5, these conditions are illustrated. To realize these constraints in code, each line constraint takes its central node as *parent* (Red) and makes the other nodes *child* (Blue) to this parent node. The parent node can translate within its specified plane which the children follow exactly, meaning rotation about the axis perpendicular to this plane is constrained. Additionally, the parent node of a line constraint becomes a child node (Brown) to the parent node of a line constraint coming exactly one revolution earlier if applicable (Purple). These line constraints are applied at every half-revolution for the planar lattice and at every quarter-revolution for the spatial lattice.

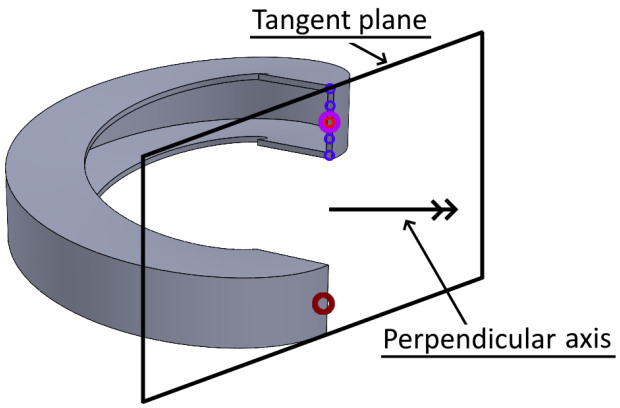

Figure 2.5: Visualization of the applied line constraints

Another constraint needed is the periodicity of the structure in consecutive revolutions. The meta-material can potentially be infinitely long, meaning that one revolution could not simulate the complete behaviour without a periodic constraint applied. This is achieved by taking the middle node of the cross-section as a parent node and making the other nodes on the cross-section child nodes. The coordinates of the child nodes are then taken with respect to the parent as *deltas*. To now apply a periodic constraint, the deltas from one end of the structure would be set equal to the deltas from the other end. This means that the deformation of the cross-section at the base would be equal to the deformation at the end of the structure, making it copy itself infinitely at its ends.

2.2.2. Optimization setup

The optimization run has an input of 6 variables: the ratio and the 5 X-coordinates of the flanges that determine its shape, as depicted in Figure 2.4. The X-coordinates of one flange will be mirrored onto the other flange to create a symmetric cross-section. The 5 Y-coordinates are set from 0.2 to 1.0 in steps of 0.2. Both the ratio and the X-coordinates would start at 1.0, simulating a U cross-section. To minimize the probability of collision between the flanges, boundary values were set between 0.5 and 1.5. These values were chosen as these would allow a maximum flange angle of 22.5 degrees, realizing a 22.5 degrees margin for certain collision of the flanges caused by deformation. To achieve a constant force (zero-stiffness) profile for the structure, the optimizer objective function is formulated as the Root Mean Squared Error (RMSE) calculated over the final 2/3 of the data points from the simulated force-displacement curve. The initial 1/3 of the data points are excluded from the analysis to account for the buildup of the settling force.

2.3. Experiment

This section details the production of the prototypes, and the testing setup that is used to validate the simulation results in section 2.2. In subsection 2.3.1 the fabrication of the prototypes is detailed. This is followed by the testing setup that is used for experimental validation in subsection 2.3.2.

2.3.1. Prototypes

In order to create the prototypes, a few 3D printing techniques were considered in Appendix D. For the final prototypes it was chosen to create the planar lattice variants, as the results for the spatial lattices currently had no constant force (zero-stiffness) solutions. The final prototypes were eventually created using Multi-Jet Fusion (MJF) with PA12 (nylon powder) as material. The reasoning behind this choice is detailed in Appendix D. In order to make sure that the meta-material is impacted minimally by its boundary effects its lattice size should be maximized. This resulted in two planar lattice prototypes: a [7 x 6] lattice and a [14 x 10] lattice, both from different optimization runs. These were the largest lattices that could be produced with the MJF fabrication method, while also fitting within the test setup. Note, that [m x n] here means m consecutive revolutions and n parallel structures. The finished prototypes can be seen in Figure 2.6, with the [7 x 6] lattice on the left and the [14 x 10] lattice on the right.

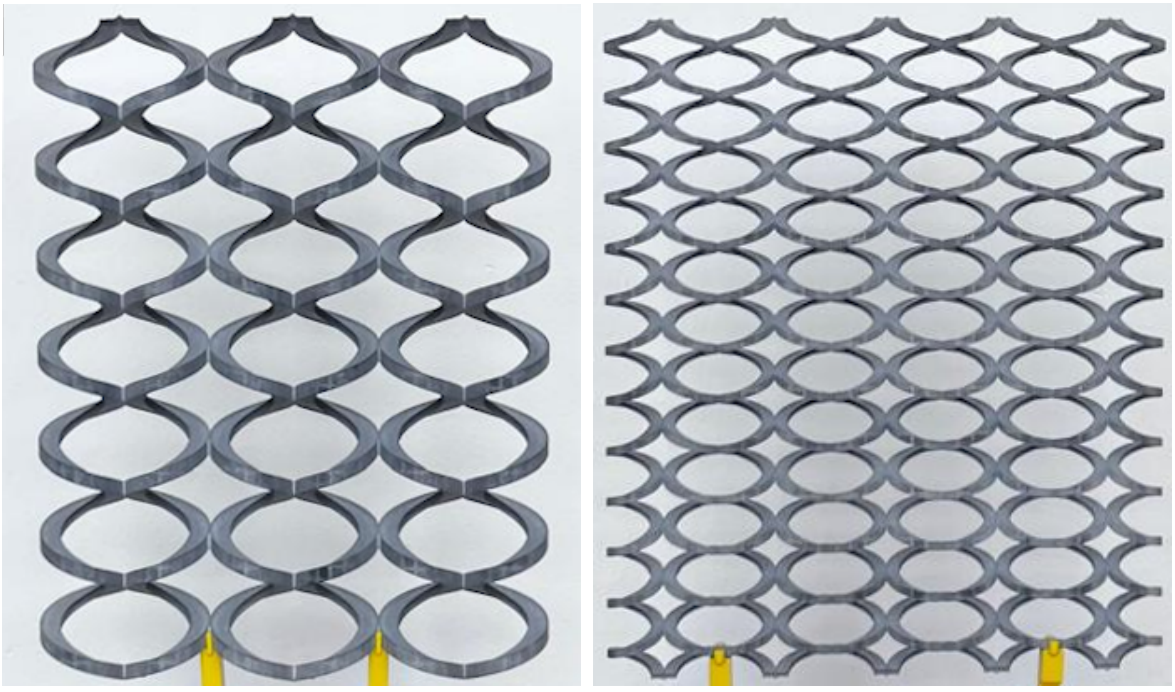

(a) [7 x 6] Prototype **(b)** [14 x 10] Prototype

Figure 2.6: Prototyped planar meta-material lattices

2.3.2. Experimental setup

For the experiment, it is important to ensure the conditions in the simulation are mirrored as closely as possible. In order to do so, the lattice should be free to expand sideways while being compressed - as the line constraints are free to move in their specified plane. Additionally, all the unit cells should be loaded equally - ideally by loading these outer unit cells with point contact. The schematic of such a setup can be seen in Figure 2.7. Here, F are fixed connection interfaces and G are guided connection interfaces.

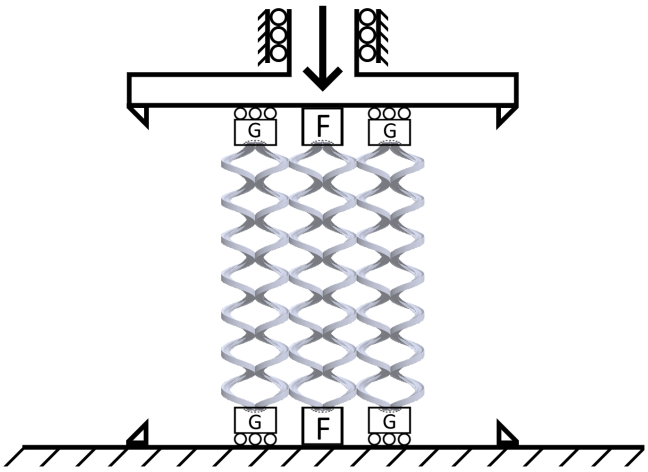

Figure 2.7: Schematic experimental test setup

Figure 2.8: Complete view test setup

The test setup was constructed by installing Thorlabs 25 mm extrusion profile at the top and bottom plate of a compression machine. Linear guide carts - with a connection interface added on top - were attached to each extrusion profile. The same was done with a fixed connection interface. The connection interfaces are pillars which have an extruded cut on them. This cut fits the outer shape of the lattice at the merged spines. This would ensure that the lattice could remain free within the connection interface while preventing it from falling or slipping out of them under actuation. Transparent acrylic plates were then mounted in front of and behind the prototypes to restrain the out-of-plane buckling of the prototypes during compression. A black piece of cloth was mounted behind the machine to provide greater contrast between the lattice and the background. Finally, a camera mounted on a tripod was positioned in front of the compression machine to film the compression of the lattices for reporting purposes. The complete setup is depicted in Figure 2.8, followed by more detailed shots in Figure 2.9 and Figure 2.10. As seen in the figures, the connection interfaces are designed to skip the upper and lower row of unit cells. This was done to prevent boundary effects from skewing the results.

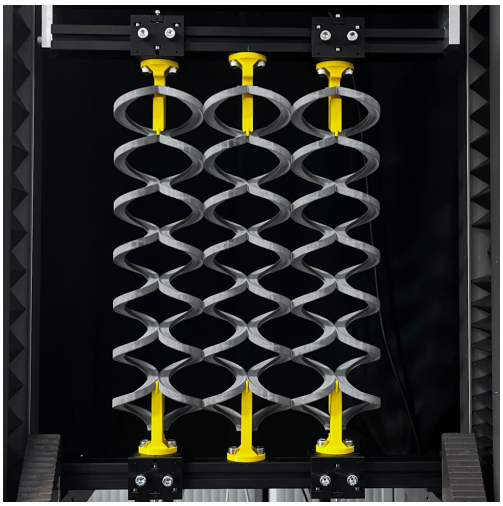

Figure 2.9: Detailed view [7 x 6] lattice test setup

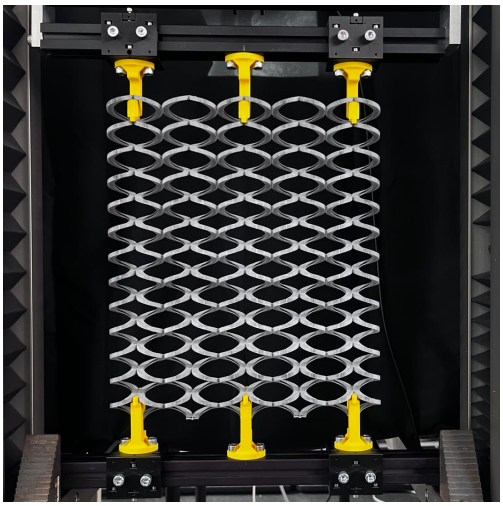

Figure 2.10: Detailed view [14 x 10] lattice test setup

3

Results

This chapter details the results that are produced during this research. It will start with the results from the optimization process in section 3.1. Here, the force-displacement curves and the optimized cross-sections of the different structures are depicted. From these optimizations, two optimized structures are selected for prototyping and testing. The results from the experiments performed on these prototypes are depicted in section 3.2.

3.1. Optimization results

Due to sizing constraints for fabrication and the desire to make the meta-material prototype contain as many unit cells as possible, three differently sized structures starting with a U cross-section were optimized. The parameters for the different types are denoted in Table 3.1. Here, h is the thickness of the structure, p is the pitch of the structure's spine, r is the outer radius of the structure (center to spine), and L is the width of the spine. Each type had two optimization runs performed on them: planar lattice configuration (half-revolution line constraints) and spatial lattice configuration (quarter-revolution line constraints) depicted in subsection 3.1.1 and subsection 3.1.2 respectively.

Table 3.1: Structure parameters per type

	h (mm)	**p (mm)**	**r (mm)**	**L (mm)**
Type 1	0.5	72	27	12
Type 2	0.5	47.5	17.8	7.9
Type 3	0.5	23.8	8.9	4.0

3.1.1. Planar lattice configuration

In Figure 3.1, the cross-sections are depicted for each planar optimization. It can be observed that all cross-sections have inward-dented features at the middle of the flanges, which corresponds to results seen from the sensitivity analysis in Appendix B. Secondary dents are observed near the edges of the different optimizations. However, the prominence of these dents seems to diminish for the smaller optimization types.

In Figure 3.2, the force-displacement curves are depicted for each planar optimization. The optimization range of the objective function is depicted with the compression marks (gray lines). For each optimization type the stiffness seems to diminish significantly. For the type 2 and type 3 optimizations a constant force (zero-stiffness) region is observed beyond the 5 mm compression mark. Looking beyond the 15 mm compression mark this region seems to be of a significant length. However, beyond the 15 mm compression mark, the flanges collide in both cases, making the results unreliable.

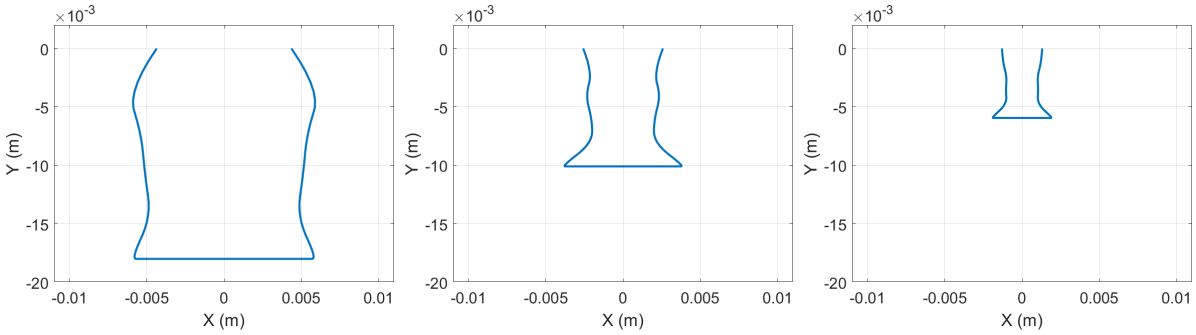

(a) Type 1 structure **(b)** Type 2 structure **(c)** Type 3 structure

Figure 3.1: Optimized cross-sections in the planar lattice configuration

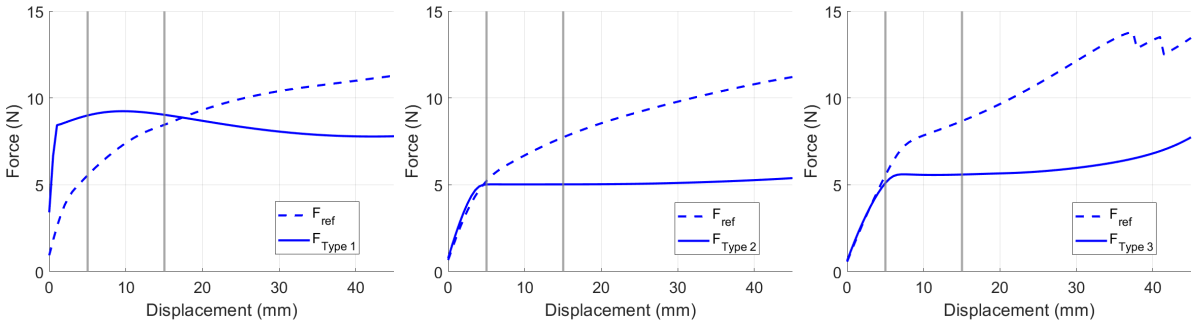

(a) Type 1 structure **(b)** Type 2 structure **(c)** Type 3 structure

Figure 3.2: Optimized force-displacement curves in the planar lattice configuration

To illustrate the compression of the structure in a planar lattice, a type 2 U cross-section structure was plotted in an undeformed and deformed state in Figure 3.3 and Figure 3.4 respectively. Here, the blue circles represent the line constraints, and the black stars represent the starting positions of certain nodes in the undeformed state.

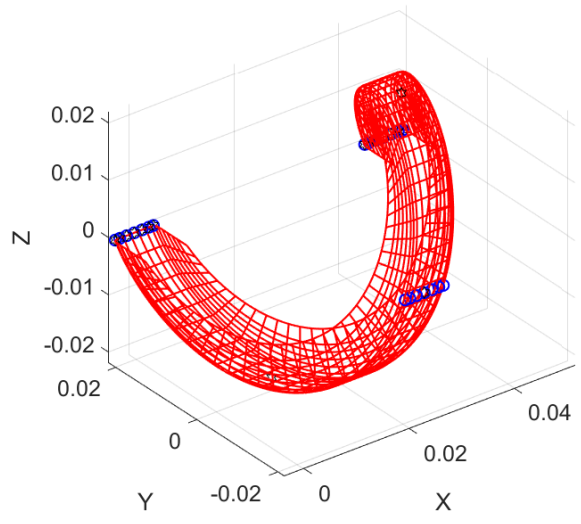

Figure 3.3: Undeformed type 2 planar structure

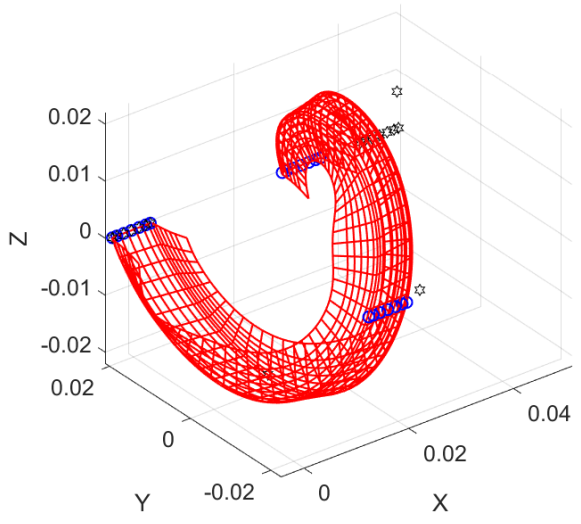

Figure 3.4: Deformed type 2 planar structure

3.1.2. Spatial lattice configuration

In Figure 3.5, the cross-sections are depicted for each spatial optimization. As can be seen in the figures, the cross-sections seem to have converged largely towards the boundary values set in the optimizer. The type 1 cross-section has fully reached the boundary values, where all settled on 0.5. The type 2 cross-section has only one parameter that is between the boundary values, with 4 having settled at 0.5 and 1 having settled at 1.5. The type 3 cross-section has two parameters that are between the boundary values, with 3 having settled at 0.5 and 1 having settled at 1.5.

In Figure 3.6, the force-displacement curves are depicted for each spatial optimization. The optimization range of the objective function is entered with the compression mark (gray line) and ends at the end of the plot. For each optimization type the stiffness seems to diminish, but not sufficient enough to realize constant force (zero-stiffness). For the type 2 structure, a sharp jump is observed in the force-displacement curve at approximately 8 mm of deformation. This jump is caused by a bistable reconfiguration of the flanges during the compression simulation.

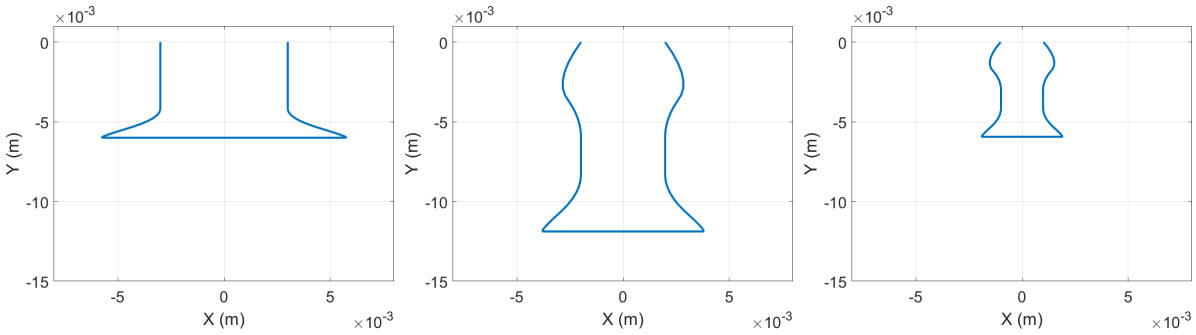

(a) Type 1 structure **(b)** Type 2 structure **(c)** Type 3 structure

Figure 3.5: Optimized cross-sections in the spatial lattice configuration

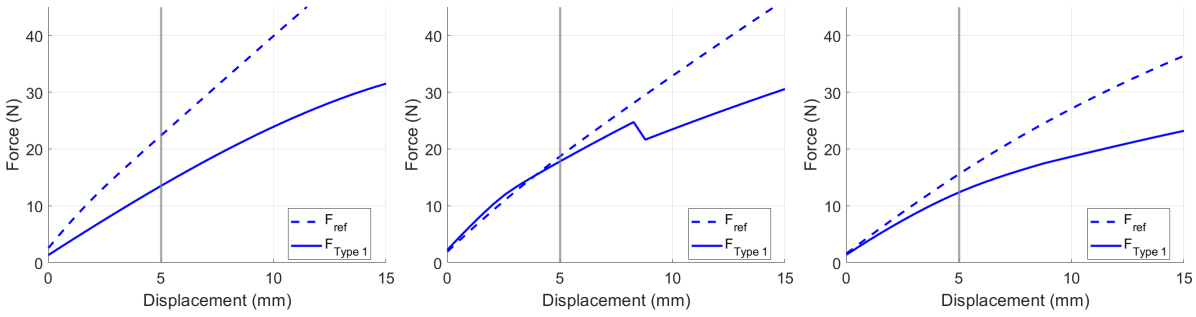

(a) Type 1 structure **(b)** Type 2 structure **(c)** Type 3 structure

Figure 3.6: Optimized force-displacement curves in the spatial lattice configuration

To illustrate the compression of the structure in a spatial lattice, a type 2 U cross-section structure was plotted in an undeformed and deformed state in Figure 3.7 and Figure 3.8 respectively. Here, the blue circles represent the half-revolution line constraints, and the green circles represent the quarter-revolution line constraints. The black stars represent the starting positions of certain nodes in the undeformed state.

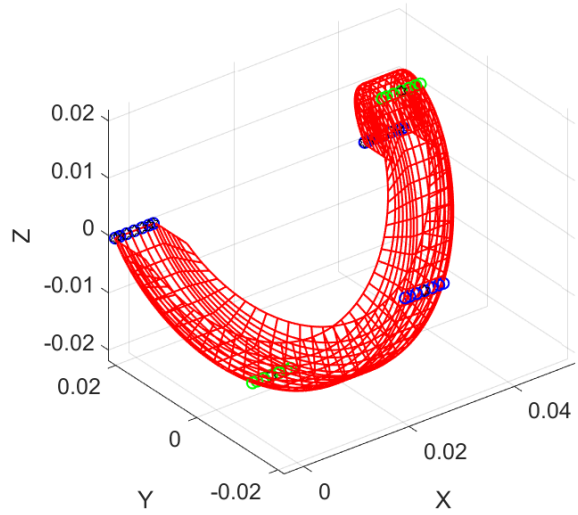

Figure 3.7: Undeformed type 2 spatial structure

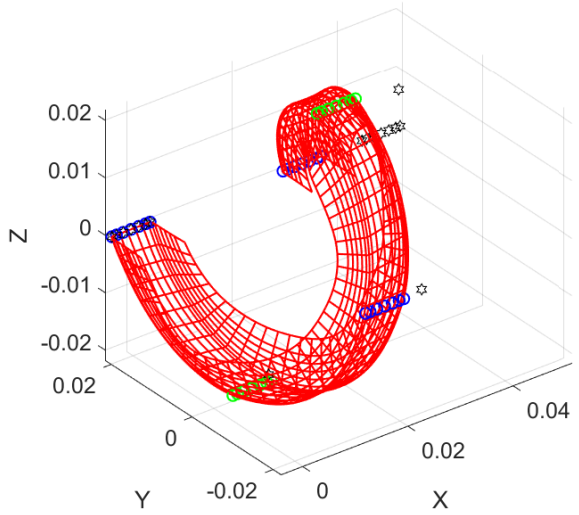

Figure 3.8: Deformed type 2 spatial structure

3.2. Experimental results

The prototypes from subsection 2.3.1 are placed in the test setup detailed in subsection 2.3.2 and compressed in several steps. The compression steps and the results are detailed in subsection 3.2.1 for the type 2 planar prototype and in subsection 3.2.2 for the type 3 planar prototype.

3.2.1. Type 2 [7 X 6] prototype

For the type 2 planar lattice, the simulation was compressed by 15 mm. Therefore, the type 2 planar prototype was compressed in incremental steps of 15 mm (0-15, 0-30, 0-45, etc.), resulting in 6 steps covering a range from 0-90 mm. Note, that this is 15 mm more than the simulated compression - which would be 75 mm for the entire lattice without boundary effects. Since the total lattice is larger than an individual structure in the simulations, the force-displacement curve for the simulations is scaled. The consecutive revolutions are springs in series, so the compression distance is scaled by 7. However, to prevent the first and last row of unit cells from exhibiting boundary effects, these are skipped. Therefore, the total compression distance is scaled by 5 instead. The adjacent structures are springs in parallel, causing the total compression force to be scaled by 6. This results in the *"Simulation"* curve. To fit the curve to the experimental data, the total force had to be scaled by the arbitrary value of 0.75, resulting in the *"Simulation - Fitted"* curve. Note, that the experimental data has a force buildup for the first 6 mm of compression, after which the curve becomes smooth. This effect is caused by the prototype sliding into the recession cut on the connection interface pillars, before being properly compressed.

3.2.2. Type 3 [14 X 10] prototype

For the type 3 planar lattice, the simulation was compressed by 15 mm. Therefore, the type 3 planar prototype was compressed in incremental steps of 15 mm (0-15, 0-30, 0-45, etc.), resulting in 9 steps covering a range from 0-135 mm. Note, that further compression to 180 mm - which would be the compression distance of the entire lattice without boundary effects - was not possible due to the limitations of the testing setup. Since the total lattice is larger than an individual structure in the simulations, the force-displacement curve for the simulations is scaled. The consecutive revolutions are springs in series, so the compression distance is scaled by 14. However, to prevent the first and last row of unit cells from exhibiting boundary effects, these are skipped. Therefore, the total compression distance is scaled by 12 instead. The adjacent structures are springs in parallel, causing the total compression force to be scaled by 10. This results in the *"Simulation"* curve. During testing it appeared that only the top half of the lattice was being compressed (see Figure 4.2), potentially caused by the out-of-plane buckling of the lattice. Therefore, the compression distance was again scaled by half of the lattice's consecutive revolutions (6/12) to fit the curve. To further fit the curve to the experimental data, the total force had to be scaled by the arbitrary value of 0.28, resulting in the *"Simulation - Fitted"* curve.

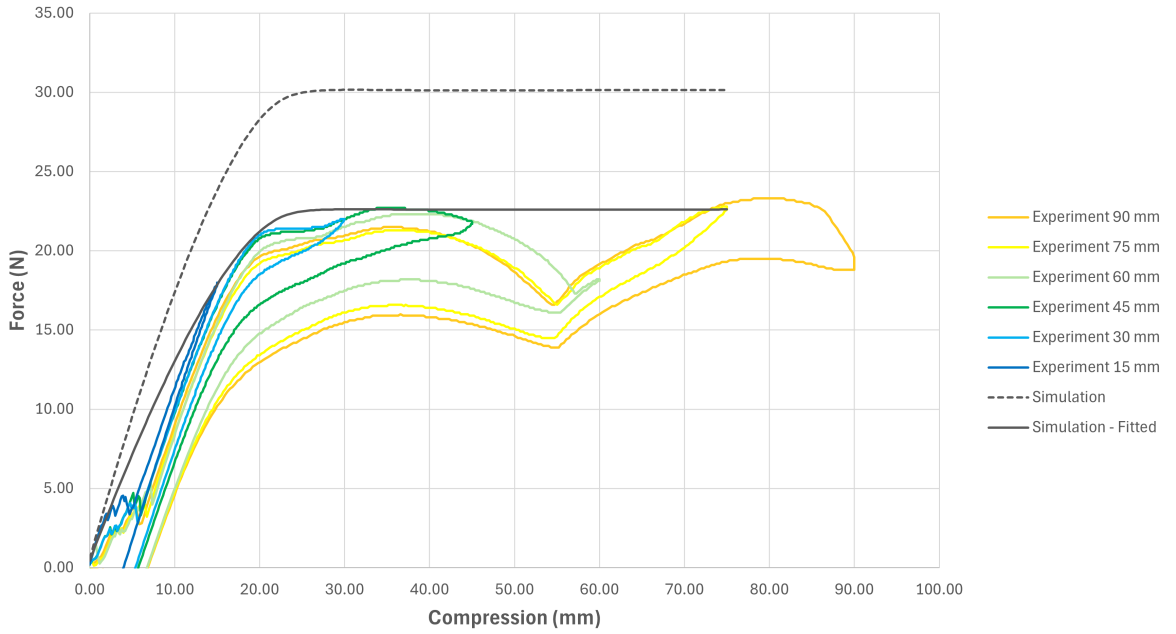

Figure 3.9: Force-displacement [7 x 6] lattice experiment

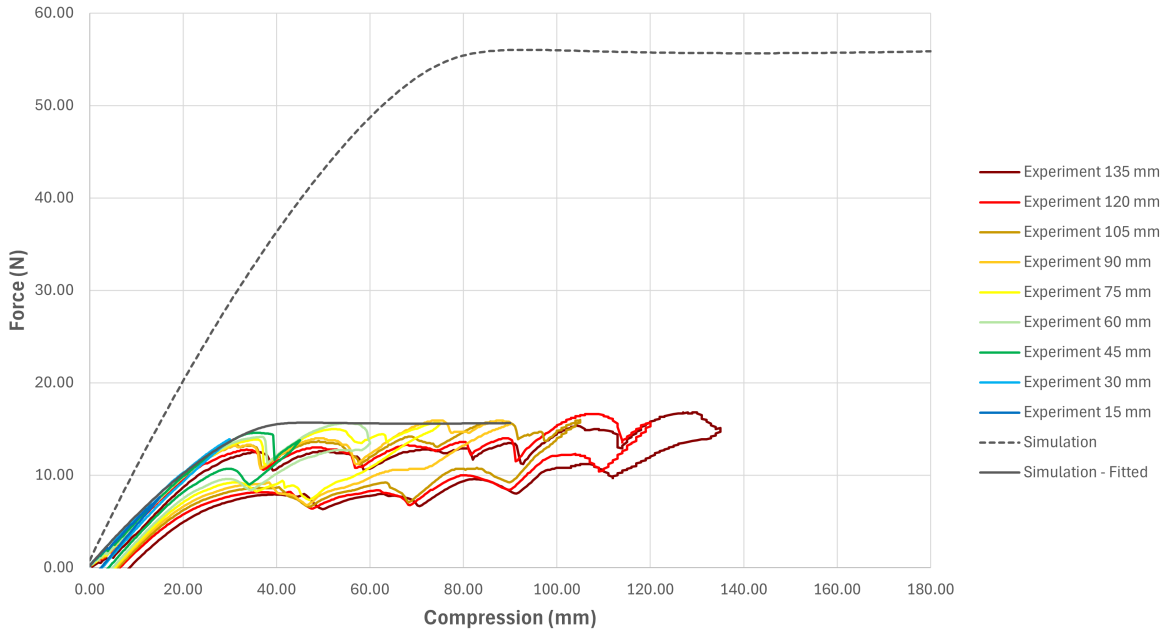

Figure 3.10: Force-displacement [14 x 10] lattice experiment

Looking at the results, it can be observed that the force-displacement curves change in consecutive tests. When a new test is performed the deformation range traced by the previous test seems to be of a lower force magnitude than before. This is caused by the visco-elastic energy storage within the material, as explained in Appendix E.

4

Discussion

Before the experimental results in section 3.2 can be compared to the simulation results in section 3.1, it is important to discuss assumptions made in this research for the simulations and optimizations, along with the limitations that were encountered during testing. First, it is assumed that each structure is deformed identically when the meta-material is compressed. However, in reality inconsistencies in production cause each individual structure within the meta-material to have somewhat different material properties and shape. Therefore, when the meta-material is being compressed, individual unit cells will enter their constant force (zero-stiffness) region at different deformations of the meta-material. This in turn can cause unit cells to be compressed further than the simulations have done, until collision occurs with itself or other unit cells. After this collision occurs, the stiffness becomes positive and the next unit cell will enter their constant force region. This causes sawtooth-like behaviour to occur with the experiments, which will be elaborated on later in this discussion. The simulations are assumed to be constructed perfectly identically, with uniform deformation over all of them. This makes it hard to predict the behaviour of the meta-material as a whole. Additionally, the absence of collision physics can cause the simulations to have larger regions of constant force than is possible in reality. Additionally, the sawtooth-like behaviour suggests that the stiffness of the unit cells becomes negative after a certain deformation, which the simulations did not show. It is therefore recommended to perform simulations where slight differences between unit cells can be accounted for. This could be achieved by simulating a few unit cells with slight variations in shape and material properties and then adding them together to simulate the result of a meta-material comprised of these units. Another option would be to simulate columns of the meta-material by not simulating 1, but several revolutions at once. This would require more computational power, as a larger mesh needs to be solved in that case. If computational power is at hand, a FEA of a complete meta-material including collision physics could provide interesting insights as well.

Second, each type of structure optimization had a total compression of 15 mm set in its simulation. Even though this is not a problem for the optimization itself, it is a problem when trying to compare the different structure types with each other. For example, the type 2 lattice is twice as large as the type 3 lattice, but both are optimized for a compression of 15 mm. Therefore, the type 3 lattice has been compressed relatively more compared to its pitch than the type 2 lattice has. Since the optimization omits the first 1/3 of data points, this results in a relatively larger settling distance of the force in the type 3 lattice than for the type 2 lattice. On the other hand, the type 3 lattice has a larger post-buckling region than the type 2 has, making it easier to optimize for a constant force (zero-stiffness) region in the first place. For example, the type 1 lattice has the lowest compression relative to its pitch, and it seems to have the hardest time converging to a constant force region compared to the other simulations, as seen in Figure 3.2. Considering these observations, it is recommended to rerun the optimizations for the type 1 and type 2 lattices with 45 mm and 30 mm of total compression respectively. This could result in better regions of constant force for these lattices, and it ensures the different types can be compared to each other in terms of relative performance.

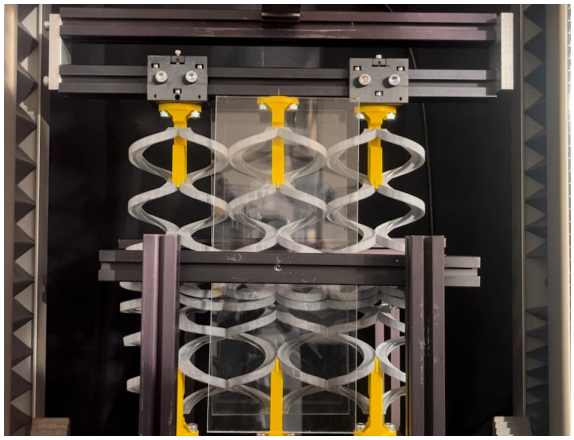

Figure 4.1: Compressed [6 x 7] lattice

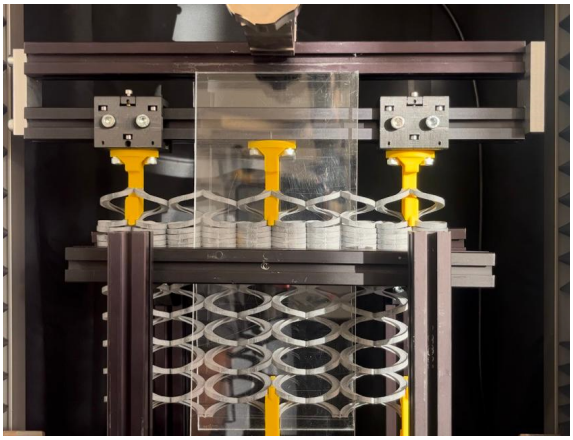

Figure 4.2: Compressed [14 x 10] lattice

Third, the out-of-plane buckling of the lattices has not been taken into account in the simulations while this is still present in the experiments. This buckling is undesired and was mostly prevented using the acrylic plates behind and in front of the lattices. As seen in Figure 4.1 for the [7 x 6] prototype and in Figure 4.2 for the [14 x 10] prototype, these measures helped for the most part. However, in the case of Figure 4.2, it seems that the friction introduced by these plates was sufficient to constrain half of the meta-material lattice. This causes only the upper half of unit cells to deform. It could be that the upper unit cells entered their constant force region (zero-stiffness) earlier by chance, but this is not likely. To combat this problem, it is strongly recommended to further this research by designing a spatial lattice meta-material with constant force unit cells, as the added relative thickness will inhibit the out-of-plane buckling. A research direction could be to try different flange geometries or adding more parameters to the optimization if computational power is available. However, since current optimizations showed little potential for a spatial lattice unit cell to work, it is advised to attempt to create a spatial lattice comprised of planar lattices with intermediate rigid links. This approach provides a multitude of orientational options to tune stiffness in all directions. One such option could be to create a meta-material that can be compressed into constant force regions in multiple directions. An example of such meta-material lattice is schematically depicted in Figure 4.3. Here, the differently colored lattices are identical and stacked into the z-direction to create a spatial meta-material. Additionally, each colored lattice could enter a constant force region by compression in the x and y direction.

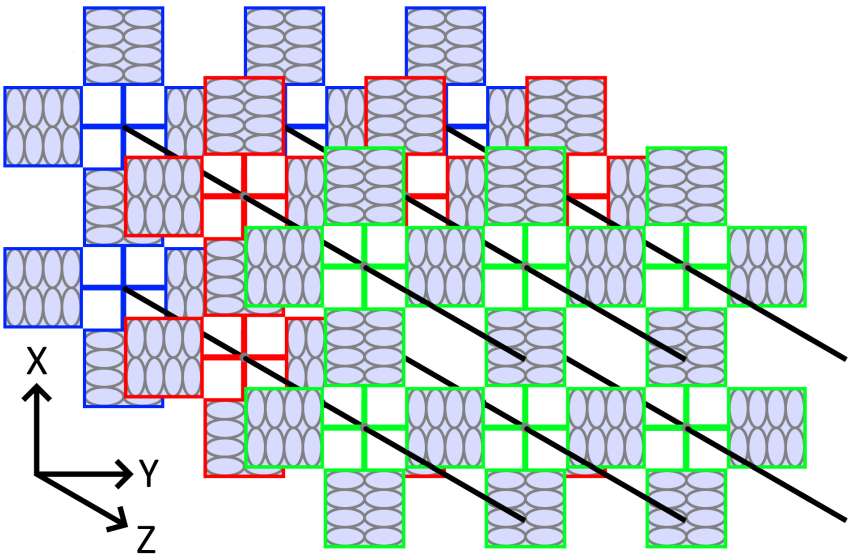

Figure 4.3: Spatial meta-material lattice comprised of planar meta-material unit cells

Lastly, the assumption needs to be addressed that neutrally stable behaviour would occur within the meta-material when its unit cells would function as constant force (zero-stiffness) springs. Earlier in this discussion it was elaborated that the small inconsistencies in production cause each individual structure to enter their constant force region at different deformations, which most likely caused the sawtooth-like behaviour seen in section 3.2. This behaviour impacts the neutral stability, as now not all unit cells will be in a constant force region under certain compressions, which was originally assumed. Furthermore, the force-displacement curves of neighboring unit cells cannot cancel each other, since the unit cells will be in other stiffness regions. To test this theory, the prototypes were compressed until the second row of unit cells entered their constant force region (the second sawtooth). The unit cells that were deformed were then moved cautiously by hand, to see if significant effort was required to propagate the deformation along the lattice. It was observed that right between the two deformed rows of unit cells a small region of neutral stability was present. Unfortunately this small region was unstable because of the sawtooth-like behaviour, causing a snap-like behaviour to occur; When attempting to move the region between the two rows, the rows would propagate one row with a snap. However, it required less effort to revert them back to the original state (middle of the meta-material lattice), making it quite unstable. Therefore, a consistent neutral stability region can currently not be achieved until a method is found to keep the unit cells in their constant force region, while neighboring unit cells enter this region as well. Considering future research where the simulations would account for the small inconsistencies mentioned before, some suggestions could be made to ensure that more rows of unit cells can be in the constant force region. If in this case the simulations indicate a region of negative stiffness after the constant force region, some sort of bumpers could be added between the unit cells which ensure early collision. This early collision would then add positive stiffness before the negative stiffness region is entered and therefore the next row of unit cells enter their constant force region. The sawtooth-like behaviour would then become smaller, making the chance of neutral stability higher in the meta-material lattice.

Keeping this in mind, the simulation results can be compared to the experimental results. First, we consider the [7 x 6] lattice seen in Figure 3.9. Scaling the numerical results to account for the lattice size and using a force magnitude modifier of 0.75, results in the *"Simulation - Fitted"* curve. This curve follows the shape of the experimental data curves if a trend line were to be drawn over the sawtooth-like behaviour discussed before. Aside from the sawtooth-like behaviours, two differences are observed between the numerical and experimental results: the magnitude and the force response for the first 8 mm of deformation. The magnitude can most likely be explained by the inconsistencies in fabrication discussed before. The difference in force response is caused by the settling of the connection interfaces onto the lattice.

Second, we consider the [14 x 10] lattice seen in Figure 3.10. Scaling the numerical results to account for the lattice size, using a force magnitude modifier of 0.28, and using a compression length magnitude modifier of 6/12, results in the *"Simulation - Fitted"* curve. This curve follows the shape of the experimental data curves if a trend line were to be drawn over the sawtooth-like behaviour discussed before. Aside from the sawtooth-like behaviours, two differences are observed between the numerical and experimental results: the compression length and the magnitude. As discussed before the lattice had significant buckling out-of-plane, keeping half of the lattice undeformed. Therefore, the compression length had to be scaled accordingly. This most likely contributed to the significant drop in force magnitude compared to the [7 x 6] lattice. Further testing is recommended to determine if this is indeed the cause.

5

Conclusion

In this research a structure is designed and optimized that exhibits a constant force (zero-stiffness) region when deformed. This is done in an effort to create a neutrally stable meta-material comprised of said structures. A novel prestressing method is used to attain a state of constant force within the structure. Here, part of the deformation range in the intended degree of freedom is exploited for prestressing. At a certain deformation level buckling will occur, causing a constant-force region to form after a certain settling force (prestress). This novel prestressing method proved to be effective and consistent without the need for tedious and expensive fabrication processes. The structure is chosen to be a U cross-section drawn over a helix, such that its flanges buckle under compression. Optimization of the structure's flanges tailored the prestress in a chosen range of motion to be sufficient to realize the constant force region. Therefore, the goal of this research is: "*To design and optimize the geometry of a coiled spatially curved shell structure in such a way that - when embedded in a meta-material lattice - they function as constant force spring. Neutral stability is then to be achieved by opposing the unit cells constant force-displacement profiles*".

Simulations of the optimized structures show promising results. Constant force (zero-stiffness) regions are observed for structures in a planar meta-material lattice, sometimes even exceeding the target regions. For a spatial meta-material lattice no constant force region is achieved with the current optimization geometries and parameters. To validate the numerical results, 2 planar lattice meta-material prototypes are made. These meta-materials are constructed using multi-jet fusion with PA12 (nylon powder) as material. One prototype consists of 7 consecutive and 6 adjacent structures. The other prototype consists of 14 consecutive and 10 adjacent structures. For this second prototype, the structure geometry parameters are about 50% the size of the other prototype, except for the thickness. A compression machine equipped with linear guides is used for the experimental validation. These guides have interfaces installed to fit the prototypes, skipping the first and last rows of unit cells to circumvent boundary effects.

The experimental results for both prototypes show sawtooth-like behaviour. These behaviours are most likely caused by small deviations in geometry and material properties between the different unit cells. Instead of all unit cells being deformed uniformly a staggered progression occurred: one row of unit cells entered the constant force region first, transitioned into the negative stiffness phase, and experienced internal collisions before the subsequent row of unit cells entered the constant force region. When a trend line is drawn over the sawtooth-like behaviour, a region of constant force (zero-stiffness) is observed. The shape of the numerical results closely match this trend line from the experiments, but there is a magnitude difference. For the [7 x 6] lattice, a scaling factor of 0.75 is required, which could partially be attributed to the fabrication inconsistencies. However, for the [14 x 10] lattice a scaling factor of 0.28 is required, which is a significant difference. This difference is most likely caused by the out-of-plane buckling that occurred for this lattice during testing. Considering both lattices needed a large scaling in magnitude and the sawtooth-like behaviour, it can be concluded that some of the assumptions made in the simulations were not accurate.

Testing the prototypes in their compressed state for neutral stability, it was observed that small and therefore unstable regions of neutral stability are found between unit cells. This behaviour could only be observed right at the transition between exiting the constant force (zero-stiffness) region of the current row of unit cells, and the next row entering this region. This is caused by the sawtooth-like behaviour: not all unit cells are at the same force region at the same time, which means the force-displacement curves are unable to cancel each other out. Further research is required to ensure unit cells enter their constant force regions, while other unit cells remain in these regions as well. This could eliminate most of the sawtooth-like behaviour, resulting in a neutrally stable meta-material. First steps in achieving this would be to improve the simulation and optimization models, such that insight into the behaviour of a unit cell is improved. This could then be used to modify the meta-material to potentially exhibit neutrally stable behaviour in the future.

References

[1] C. Soukoulis and M. Wegener, "Past achievements and future challenges in the development of three-dimensional photonic metamaterials," *Nature Photonics*, vol. 5, pp. 523–530, Jul. 2011. DOI: 10.1038/nphoton.2011.154.

[2] E. Barchiesi, M. Spagnuolo, and L. Placidi, "Mechanical metamaterials: A state of the art," *Mathematics and Mechanics of Solids*, vol. 24, pp. 212–234, 1 Jan. 2019, ISSN: 17413028. DOI: 10.1177/1081286517735695.

[3] L. L. Howell, "Compliant mechanisms," in *21st Century Kinematics*, J. M. McCarthy, Ed., London: Springer London, 2013, pp. 189–216, ISBN: 978-1-4471-4510-3.

[4] P. R. Kuppens, "Energy invariant mechanisms," Jun. 2021. DOI: https://doi.org/10.4233/uuid:579b7c68-8c13-493c-87d9-0f77d5fba34c. [Online]. Available: https://repository.tudelft.nl/record/uuid:579b7c68-8c13-493c-87d9-0f77d5fba34c.

[5] M. Schenk and S. Guest, "On zero stiffness," *Proceedings of the Institution of Mechanical Engineers, Part C: Journal of Mechanical Engineering Science*, vol. 228, pp. 1701–1714, 10 2014, ISSN: 20412983. DOI: 10.1177/0954406213511903.

[6] I. Kuder, A. Arrieta, W. Raither, and P. Ermanni, "Variable stiffness material and structural concepts for morphing applications," *Progress in Aerospace Sciences*, vol. 63, pp. 33–55, Nov. 2013, ISSN: 0376-0421. DOI: 10.1016/J.PAEROSCI.2013.07.001.

[7] S. Guest, E. Kebadze, and S. Pellegrino, *A zero-stiffness elastic shell structure*, 2011. [Online]. Available: https://msp.org/jomms/2011/6-1/p14.xhtml.

[8] C. Ren, D. Yang, and H. Qin, "Mechanical performance of multidirectional buckling-based negative stiffness metamaterials: An analytical and numerical study," *Materials*, vol. 11, 7 Jun. 2018, ISSN: 19961944. DOI: 10.3390/MA11071078. [Online]. Available: https://www.researchgate.net/publication/325982720_Mechanical_Performance_of_Multidirectional_Buckling-Based_Negative_Stiffness_Metamaterials_An_Analytical_and_Numerical_Study.

[9] G. Radaelli and J. Herder, *Gravity balanced compliant shell mechanisms*, 2017. DOI: https://doi.org/10.1016/j.ijsolstr.2017.04.021. [Online]. Available: https://www.sciencedirect.com/science/article/pii/S0020768317301737.

[10] S. Kok, G. Radaelli, A. A. Nobaveh, and J. Herder, "Neutrally stable transition of a curved-crease planar shell structure," *Extreme Mechanics Letters*, vol. 49, p. 101 469, Nov. 2021, ISSN: 2352-4316. DOI: 10.1016/J.EML.2021.101469.

[11] J. Zhu, G. Radaelli, and J. Herder, "Towards a neutrally stable compressible metamaterial," Mar. 2024. DOI: https://resolver.tudelft.nl/uuid:a93d4da4-ce95-4932-9293-4adcc95a2966.

[12] A. Nagy, M. Abdalla, and Z. Gurdal, "Isogeometric design of elastic arches for maximum fundamental frequency," *Structural and Multidisciplinary Optimization*, vol. 43, pp. 135–149, Aug. 2011. DOI: 10.1007/s00158-010-0549-z.

[13] M. Zurik, *Sla vs. sls: Polymer 3d printing technologies*. [Online]. Available: https://www.protolabs.com/en-gb/resources/blog/stereolithography-versus-selective-laser-sintering/.

[14] *Mjf vs sls 3d printing – a head-to-head comparison*. [Online]. Available: https://www.protolabs.com/en-gb/resources/design-tips/mjf-vs-sls-3d-printing-a-head-to-head-comparison/.

A

Concept evaluation

This appendix details the preliminary research phase of this research, where several approaches are considered to reach zero-stiffness in a structure. The concept exploration is detailed in section A.1, followed by the evaluation of all the concepts in section A.2. Here, it is concluded that the optimization of the cross-section would be most suitable to attain constant force (zero-stiffness) for this research.

A.1. Concept exploration

Different approaches are considered with which constant force (zero-stiffness) could be reached. These ranged from prestressing a singular structure, to assembling a meta-material in such a way that the meta-material as a whole is prestressed. The methods that are considered to realize the constant force using coiled spatially curved shell structures are:

1. Forcing a bistable state using hinges in the structure's cross-section.
2. Prestressing the structure by using tensioning cables along their profile.
3. Prestressing the structure by sleeving it with slightly smaller versions of said structure.
4. Prestressing a meta-material by pretwisting the individual structures before assembly.
5. Optimizing the structure's geometry in such a way that it realizes a constant force state for the entire meta-material when actuated.

Here options 1-3 would focus on realizing constant force (zero-stiffness) within the structure on its own, whereas the 4 & 5 focused on realizing the constant force within the structure in a meta-material lattice.

A.2. Concept evaluation

To narrow down the scope of the research, a few simple prototypes are made to test the different approaches on their feasibility. To rate the feasibility of each approach, a few factors are considered:

- The factor of stiffness reduction.
- The amount of manual hours needed to fabricate this method.
- The propriety of the method for making a meta-material lattice with it.
- The propriety of the method for miniaturization.

Method 1 is prototyped by cutting open a cardboard toilet roll, and then forcing it into a bistable warped state. This is achieved by adding hinges that are slightly larger than the gap size on the opposing sides as depicted in Figure A.1. Since the cross-section tends to keep the gap as closed as possible, it would warp. The nature of the hinges made sure that it could warp in two ways, creating the bistable

warped state. This is useful since bistability can often be tuned to zero-stiffness[5]. The prototype did unfortunately show that after some time, the cross-section ceased to warp and deformed instead. This resulted in a larger gap size. This could potentially be fixed by thickening the shell at its neutral axis. However, this was never explored further, as the method had already been abandoned due to other challenges with this method. The main challenges were producing it in a miniaturized or latticed manner for meta-materials. It must be noted that this might still be interesting to research further in the future, as it might have potential applications that have not been discovered yet.

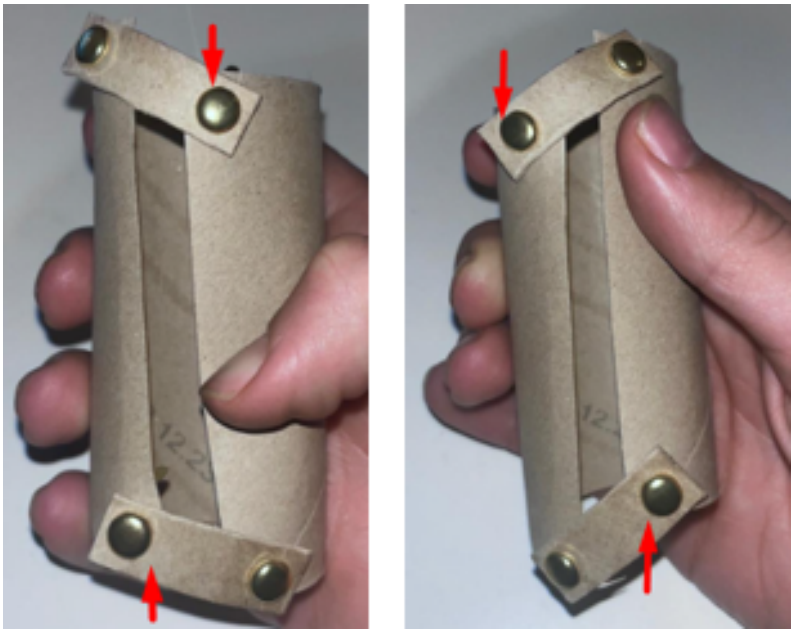

Figure A.1: Cardboard prototype forced into warping

Method 2 is prototyped using FDM based 3D printing to create a shell. This shell has a U cross-section and has small rings on the inner radius to lead a wire through. Applying this wire was a tedious process and unwanted effects occurred. For one, the structure is forced into a smaller radius. This resulted in nonconstructive stress within the structure that "locked" it into its current orientation. This method was abandoned, as it yielded too little results for a significant manual labor to fabricate the shell. It must be noted that wires cured within a polymer matrix could still be useful to create the desired structure. However, for this research these resources were not readily available.

Method 3 is prototyped using FDM based 3D printing to create two shells. These shells have a U cross-section and are printed in a larger and smaller size. The smaller sized shell is then fitted around the larger sized shell, prestressing them both. The behaviour of the shells are affected, but not significant enough to indicate that zero-stiffness could be attained in some way using this method. Additionally, it would be hard to realize this in a lattice in the future. Therefore, this method was abandoned for further investigation.

Method 4 is prototyped using FDM based 3D printing to create four shells. These shells have a U cross-section, and are arranged into a grid. Therefore, 2 shells have to be mirrored versions of the other 2. The 4 shells are attached to the same baseplate as depicted in Figure A.2, and then pretwisted. The pretwist is then locked by attaching a top-plate to the 4 shells. This realized prestress in a relatively easy manner for this lattice size. The effects of bistability are observed within the windings of each shell, which proved that this might be a viable method. One issue with this method is that the individual windings are free to move around, creating a lot of internal DoF. These could be attached to the windings of the other shells on the same level, but this would be a tedious task on smaller scales. These challenges caused this method to be abandoned for this research.

Figure A.2: Printed forced pretwist prototype

Method 5 is prototyped using FDM based 3D printing to create an entire meta-material consisting of a shell with a U cross-section. Here, the structure's flanges are altered to change its stiffness properties. It was observed that for different flange angles and structure geometries the buckling behaviour is changed at the flanges when the meta-material is elongated or compressed. This indicated that with the correct geometry constant force (zero-stiffness) could potentially be reached. It took some manual labor to remove supports for the prints, but with other printing methods this could be reduced. Additionally, no assembly is needed, making miniaturization viable for this method as well. Therefore, method 5 is chosen as the fundamental basis for this research.

B

Parameter sensitivity analysis

This appendix details the parameter sensitivity analysis that is performed in order to determine which parameters are most suitable for the optimization process. The parameters considered are detailed in section B.1, followed by the evaluation of all the results in section B.2.

B.1. Parameters

The parameters that are considered are visually shown in Figure B.1 and listed below:

- The thickness of the structure h
- The pitch of the structure p
- The outer radius of the structure (center to spine) r
- The width of the spine L
- The length of the flanges (l) w.r.t. the width of the spine (L) as ratio
- The angle of the flanges w.r.t. the spine θ
- The general shape of the flanges

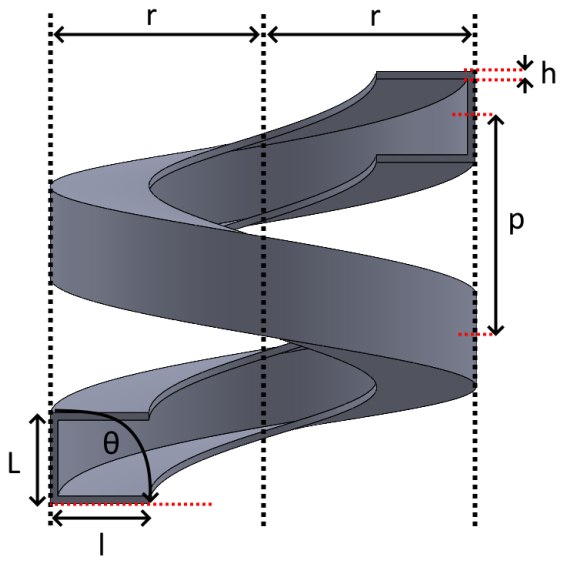

Figure B.1: Parameters determining geometry

A reference simulation is performed where the structure is compressed by 15 mm. Here, the parameters are: h = 0.5 mm, p = 72 mm, r = 27 mm, L = 12 mm, ratio = l/L = 1, $\theta = 90°$, and the flanges are straight. Each parameter is varied to 2/3 and 4/3 of these original values separately, with an exception of the flange angle and flange shape. The flange angle is changed to lower than and higher than 90° instead, and the flange shape is varied from straight to dented inwards and dented outwards.

B.2. Analysis Results

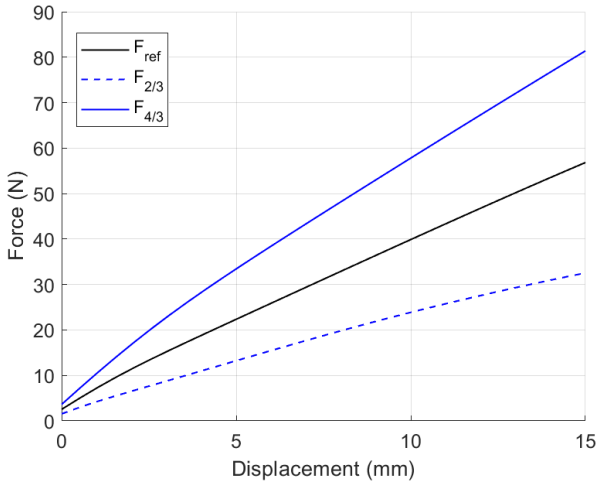

Figure B.2: Parameter variation of h

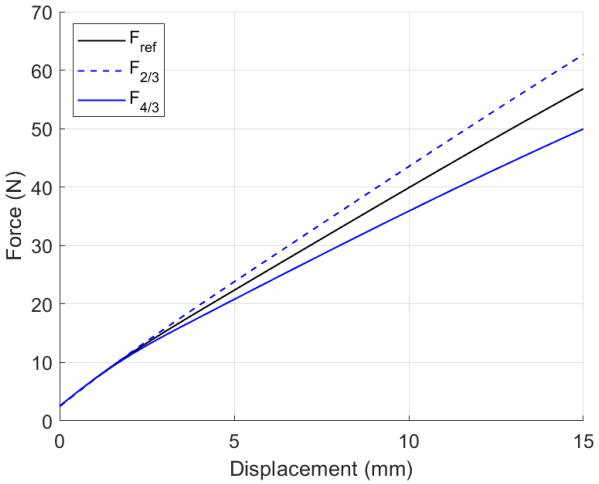

Figure B.3: Parameter variation of p

As seen in Figure B.2, the thickness h affected the stiffness, but its usability is limited. It scales the overall required force down by lowering h, which can be useful. However, the fabrication method must then allow for smaller thicknesses.

As seen in Figure B.3, the pitch p affected the stiffness, with a higher pitch flattening the force curve. This could be used to reach constant force (zero-stiffness), but the size constraints should be considered. This is because a larger pitch significantly increases the unit cell size.

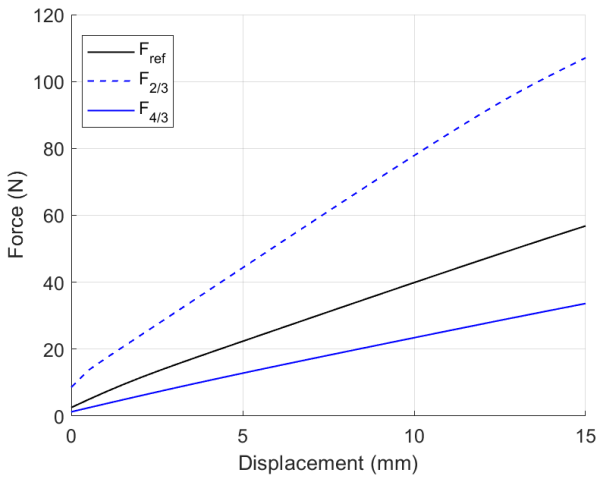

Figure B.4: Parameter variation of r

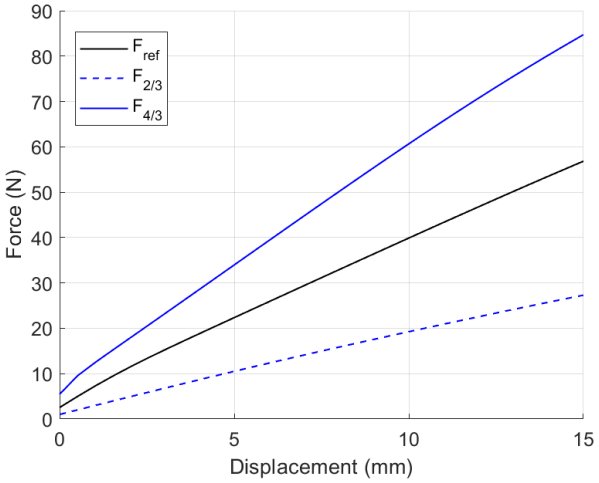

Figure B.5: Parameter variation of L

As seen in Figure B.4, the radius r affected the stiffness, but its usability is limited. It can lower the overall required force by increasing the radius, but this would enlarge the unit cell significantly. This means that size constraints need to be considered.

As seen in Figure B.5, the spine width L affected the stiffness, but its usability is limited. It scales the overall required force down by lowering L. However, the fabrication method must then allow for less space between the flanges, if supports are needed.

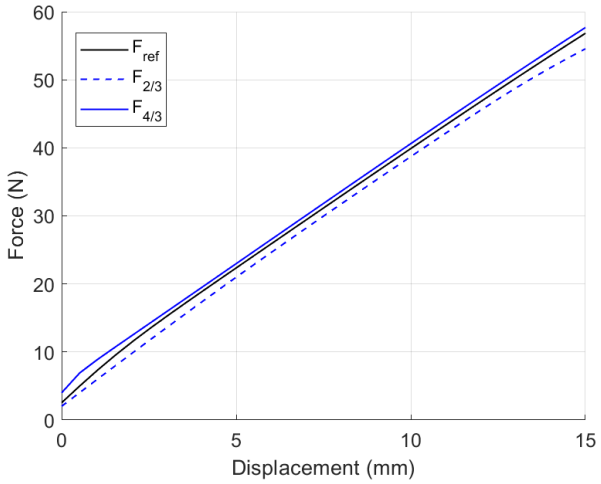

Figure B.6: Parameter variation of ratio

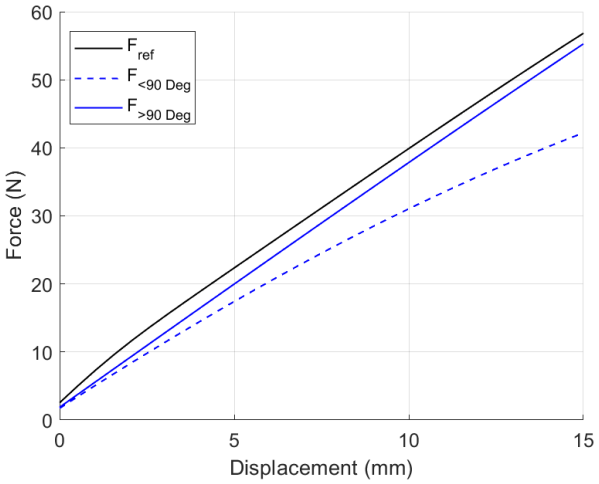

Figure B.7: Parameter variation of flange angle θ

As seen in Figure B.6, the ratio (l/L) has almost no effect on the stiffness. However, it is theorized that the ratio will have a more significant effect when the flange shape is changed as well. Therefore, an analysis combining these two parameters can be found further down.

As seen in Figure B.7, the flange angle θ flattens the force curve when θ becomes smaller. This can only be used to a certain extent, as values lower than 45 degrees will cause the flanges to collide with each other. Even though collision means nothing in the simulations (as it does not exist), it will change the stiffness characteristic for a real prototype. Furthermore, when deformation occurs, the flanges bend inwards. This means a higher bound than 45° is desired (if ratio >= 1), when this parameter is optimized.

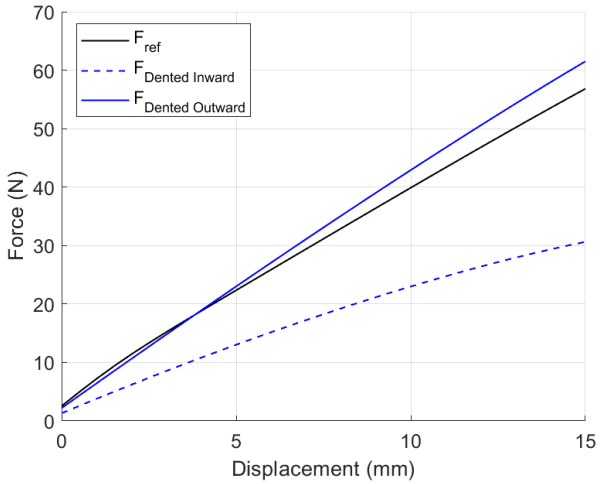

Figure B.8: Parameter variation of flange shape

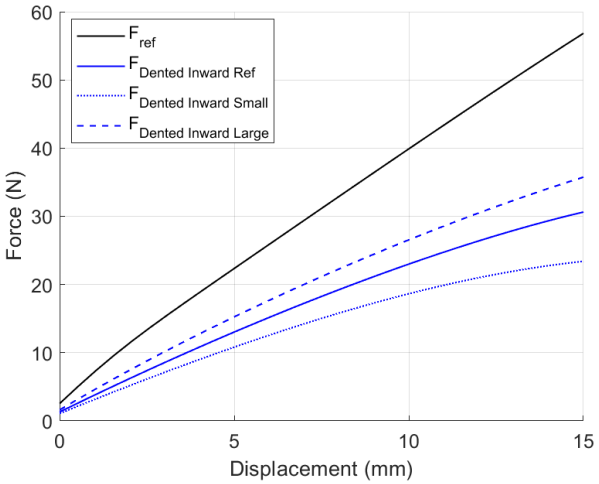

Figure B.9: Parameter variation of flange shape & ratio θ

As seen in Figure B.8, the flange shape flattens the force curve significantly when the flanges are dented inwards. This is a viable option to change the stiffness curve towards zero, but some caution should be taken. Similar to aforementioned flange angle, denting the flanges inwards increases the risk of collision of the flanges. However, here the risk is somewhat lower than that for the flange angle, as the midpoints of the flanges and not the edges of the flanges are closest together in this case.

As mentioned before in the ratio section, it is theorized that the ratio might play a bigger role when the flange shape is also altered. Since the inward dented shape is observed to have better results than the flange angle, it was simulated together with a varying ratio. In Figure B.9, it is clear that the curve can be flattened even more if the ratio - and by extension the flange length - is made smaller. This shows that the ratio still might be a good parameter to optimize for, contrary to what the first results had shown.

Concluding this sensitivity analysis, it is decided that for the optimization process in this research only two parameters have to be optimized. First, the shape and angle of the flanges seem to impact the stiffness behaviour the most efficiently. It is decided that these two parameters could be coupled into one: node points of a spline creating the cross-section. The secondary parameter chosen is the ratio, as this seems to have a significant effect when a flange is not straight. The other parameters could be interesting to optimize for in the future if the fabrication method allows for the changes in size and the computational power is available.

C

Other optimizations

This appendix details additional optimization runs that are performed in hopes of achieving better results for primarily the spatial lattice. In the main report only symmetric flanges are considered. In this appendix, parallel flanges in section C.1, variable angle flanges in section C.2, and having only a singular flange in section C.3 are detailed. For each flange type, two optimization runs are performed where both start from a type 1 structure with a U cross-section. The first run is for the planar lattice configuration, and the second one is for the spatial lattice configuration.

C.1. Parallel flanges

For this optimization, the flanges are parallel instead of mirrored. This makes the cross-section asymmetric instead of symmetric. For the type 1 planar structure the optimized cross-section is depicted in Figure C.1. The resulting force-displacement curve upon compression is seen in Figure C.2. As seen in the figure: the stiffness seems to diminish significantly, but is not completely flat yet, with respect to the general U cross-section reference. Additionally, the total required compression force is somewhat higher at around 8 N than the optimizations in subsection 3.1.1.

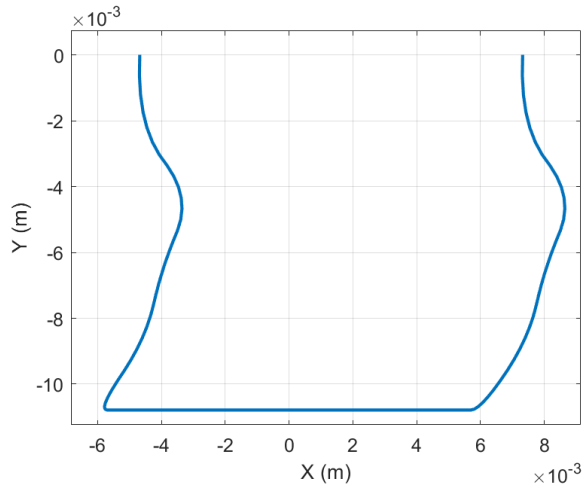

Figure C.1: Cross-section of type 1 structure in planar lattice

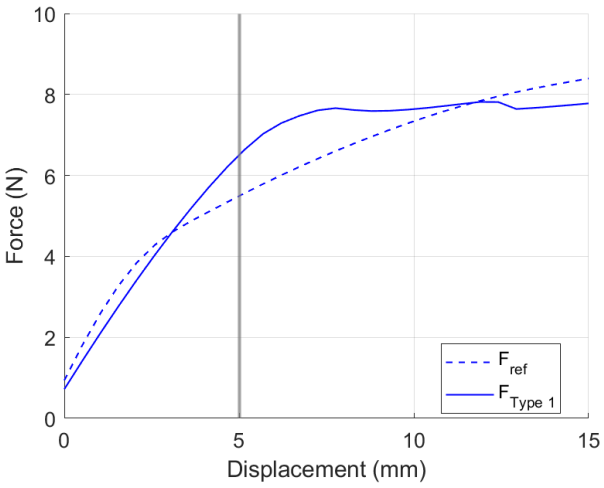

Figure C.2: Forces of type 1 structure in planar lattice

For the type 1 spatial structure the optimized cross-section is depicted in Figure C.3. The resulting force-displacement curve upon compression is seen in Figure C.4. As seen in the figure: the force-displacement curve seems to have a small softening effect. At 13 mm of deformation, the stiffness even inverts. This can potentially be improved by changing the boundary values, as 2 out of the 6 optimized values ended at 0.5 and 2 ended at 1.5. This means 2 values were optimized between the boundary values. Changing the 0.5 optimizer boundary value is unfortunately not an option, as collision between the flanges is then unavoidable.

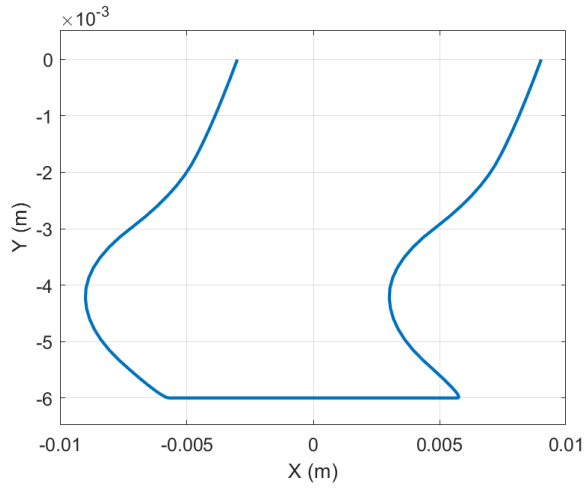

Figure C.3: Cross-section of type 1 structure in spatial lattice

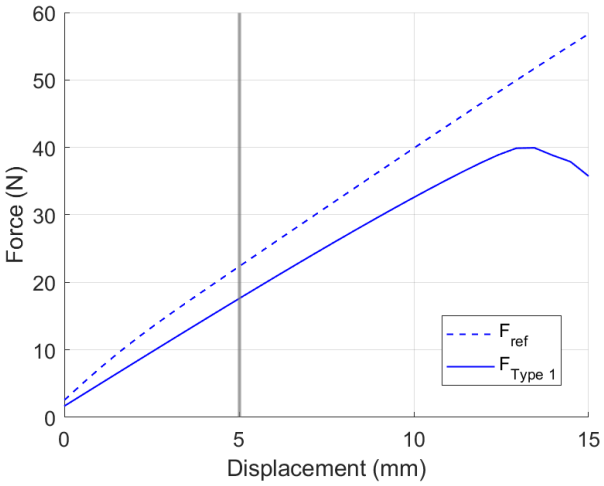

Figure C.4: Forces of type 1 structure in spatial lattice

C.2. Variable angle flanges

For this optimization, the flange angles are varied along the helix instead of being constant. This was achieved by adding a sinusoid with an amplitude of L/4 to the X-coordinates of the cross-section along the helix. The period of the sinusoid was set equal to π making it fit twice within one revolution. For the type 1 planar structure the optimized cross-section is depicted in Figure C.5. The resulting force-displacement curve upon compression is seen in Figure C.6. As seen in the figure: the force-displacement curve flattens with respect to the general U cross-section reference. Additionally, the total required compression force is somewhat higher at around 8 N than the optimizations in subsection 3.1.1.

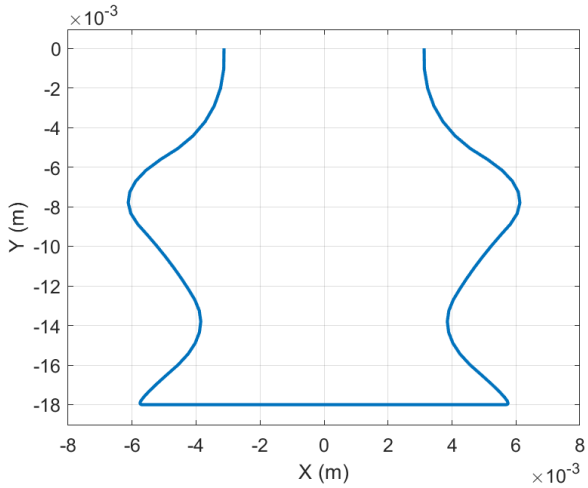

Figure C.5: Cross-section of type 1 structure in planar lattice

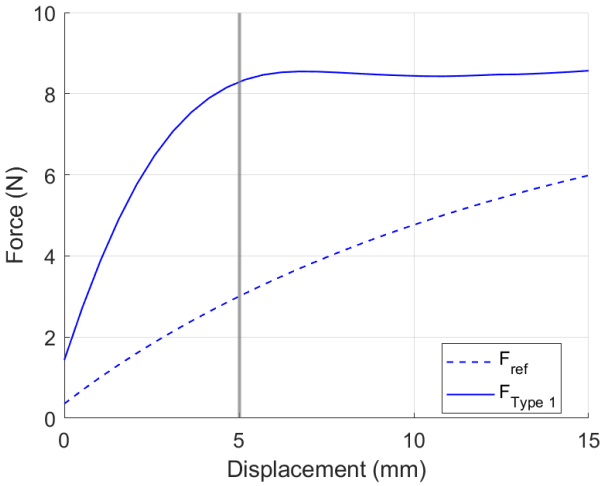

Figure C.6: Forces of type 1 structure in planar lattice

For the type 1 spatial structure the optimized cross-section is depicted in Figure C.7. The resulting force-displacement curve upon compression is seen in Figure C.8. As seen in the figure: the force-displacement curve has a softening behaviour, but is not close to flattening yet. This could potentially be improved by changing the boundary values, as the optimized values all ended at 0.5. Lowering this optimizer boundary value is unfortunately not an option, as collision between the flanges is then unavoidable. Another thing of note is that the curve has a sharp jump around 14 mm of deformation. This is caused by a bistable reconfiguration of the flanges during the compression simulation.

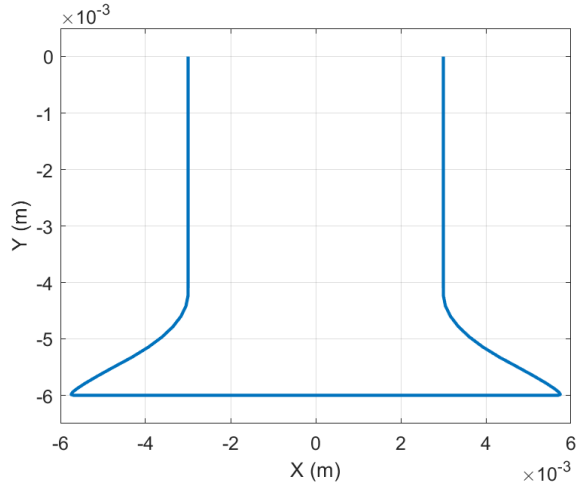

Figure C.7: Cross-section of type 1 structure in spatial lattice

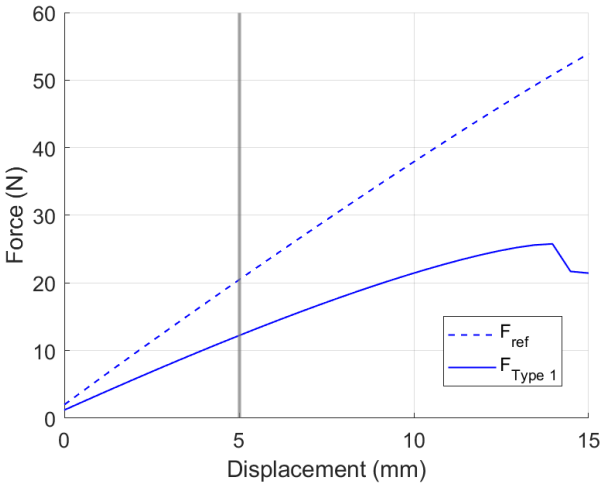

Figure C.8: Forces of type 1 structure in spatial lattice

C.3. Singular flange

For this optimization, there would be only one flange instead of two. This would make the cross-section asymmetric instead of symmetric. For the type 1 planar structure the optimized cross-section is depicted in Figure C.9. The resulting force-displacement curve upon compression is seen in Figure C.10. As seen in the figure: the force-displacement curve flattens more efficiently than intended, as it reaches this plateau earlier than the 5 mm compression mark. Additionally, the total required compression force is somewhat lower at around 3 N than the optimizations in subsection 3.1.1.

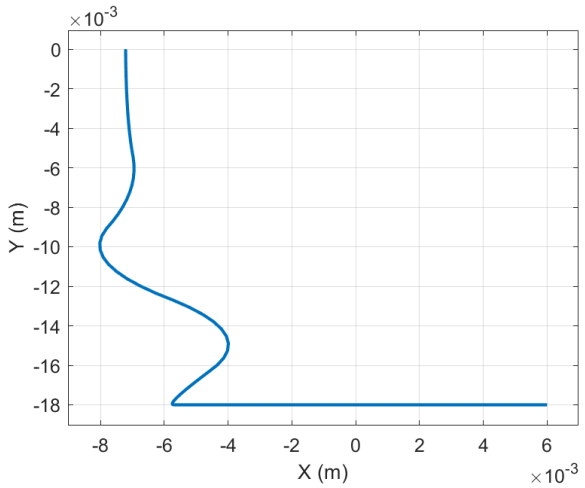

Figure C.9: Cross-section of type 1 structure in planar lattice

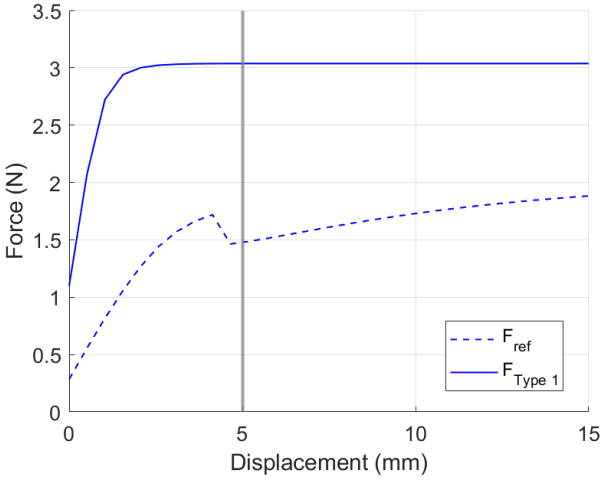

Figure C.10: Forces of type 1 structure in planar lattice

Unfortunately, the spatial optimization did not converge. Therefore, only results for the planar lattice are presented. It might be interesting to try an optimization for the spatial lattice with a more refined mesh in the future if the computational power is available.

C.4. Remarks

Looking at the different types of simulations that were performed, there are a few things that can be seen. Firstly, the planar lattices do seem to come near constant force (zero-stiffness) regions. However, except for the singular flange variant, they are not as efficient as the symmetrical variants - which reached the target constant force plateau earlier than these optimizations. Additionally, the curves are smoother for the optimizations performed in subsection 3.1.1. Therefore, the optimizations for the symmetrical (mirrored) flanges were chosen to be prototyped. This leaves the question why the singular flange variant is not chosen, as these outperformed the symmetrical flanges. The reason is that the singular flange variant was thought of and optimized after the prototypes were ordered. This was done in hopes of achieving better results for the spatial variant. In future research to enhance the performance it is recommended to explore prototyping the singular flange variant instead of the symmetrical optimization. Secondly, for the spatial lattices it seems constant force is significantly harder to reach than for the planar variants. While softening behaviour is often present it is not sufficient to cancel out the positive stiffness present. More research needs to be dedicated to other geometries or parameters to ascertain whether it is possible to create a constant force spatial lattice using the flange optimization method.

D

Fabrication Methods

This appendix details the several fabrication methods that are considered to create the final prototype. The different fabrication methods are categorized as follows: FDM printing in section D.1, SLA printing in section D.2, SLS printing in section D.3, and MJF printing in section D.4.

D.1. FDM printing

Fused Deposition Modeling (FDM), was considered since it is the most available technology. Prototypes were printed on a Bambu Lab X1-Carbon using PLA and PET-G filaments. The resulting prints are depicted in Figure D.1 and Figure D.2 respectively. The wall thickness of these prints is a singular printing line due to the thin-walled features (0.5 mm). This caused delamination to occur during compression quite quickly. It was therefore concluded that if FDM printing was to be used, a tougher filament, smaller nozzle size, and/or post-processing was/were needed for a qualitative print.

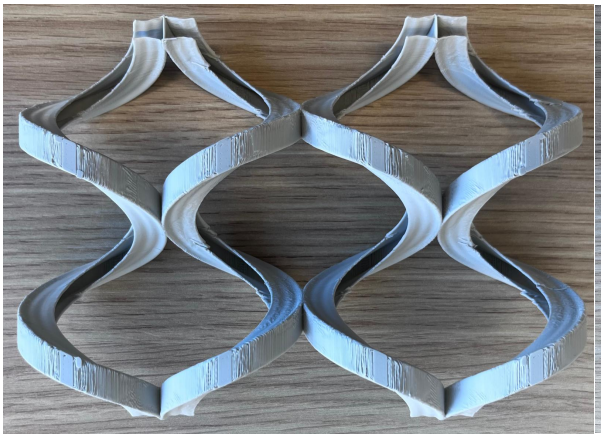

Figure D.1: PLA prototype

Figure D.2: PET-G prototype

For this research, a smaller nozzle was not available. Therefore, it was chosen to select a tougher filament instead. PA (nylon) filament would be ideal for these specifications and was therefore selected for the next test print. This proved difficult to print because of PA's hydrophilic nature and the absence of a drying chamber during printing. Eventually the print depicted in Figure D.3 was created. This print was far from perfect, with tears in the flanges and stringy material coming from the meta-material itself. However, for initial testing of the meta-material it proved to work. FDM printing was eventually still abandoned for final prototyping, as the print quality did not suffice for the final prototype using the available nozzles and filaments.

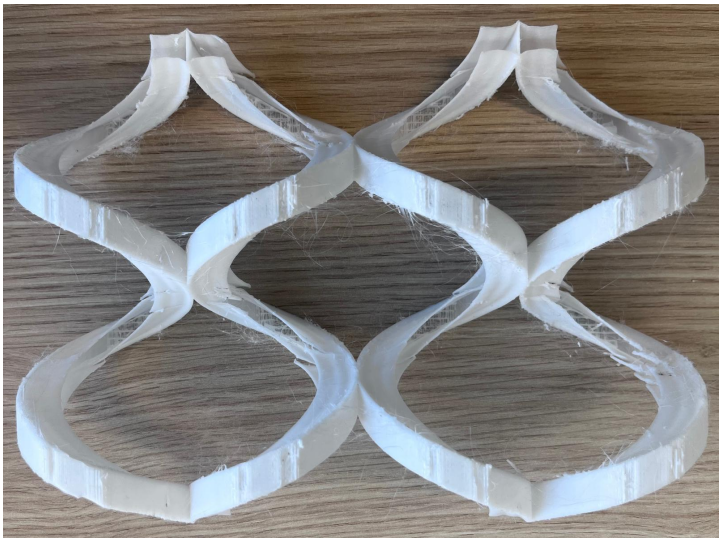

Figure D.3: PA prototype

D.2. SLA printing

Stereolithography (SLA) was considered after FDM printing, as its feature resolution is significantly higher than that of FDM. This could solve the delamination issue while improving the quality of the print itself. A prototype was made with a Formlabs Form 3 printer using Tough 1500 resin. The resulting print is depicted in Figure D.4. The print was quite smooth so delamination was no issue, but there were other issues with this print. For example, the cross-section had deformed during curing as it bended under its own weight before hardening out. Additionally, the supports - seen in Figure D.5 - were hard to remove without damaging the flanges, since the features are small. In order to improve this print, more supports are needed and an easier way to remove said supports. Soluble supports might solve these issues, but would increase the production cost significantly as another printer - the Stratasys J5 MediJet - with more expensive resins would then be needed. SLA printing was therefore abandoned for final prototyping, as there still are a lot of issues to solve with production cost already being quite high compared to other methods.

Figure D.4: SLA prototype

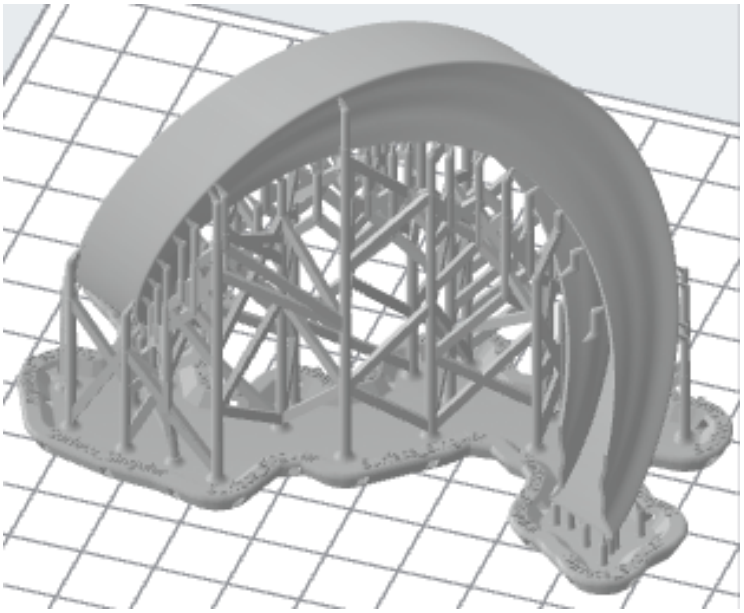

Figure D.5: Supports for SLA print

D.3. SLS printing

Selective Laser Sintering (SLS) was also considered after FDM printing. The feature resolution of SLS is significantly higher than that of FDM but lower than that of SLA. The key difference is that SLS creates more durable prints than SLA does, making it usable for this application[13]. However, SLS is a more expensive method than SLA. Using the SLS method the structure could be made from metals or plastics such as PA. As mentioned in section D.1 PA was a suitable option, while also being cheaper then metal options. Therefore, it was decided that SLS could be a suitable printing method using a PA granulate, even though it would be more expensive.

D.4. MJF printing

Multi-Jet Fusion (MJF) was considered when SLS was selected as a suitable candidate for printing, since it is quite similar to it. The key difference is that MJF has a slightly better resolution, while also being cheaper than SLS[14]. SLS does have a broader range of material choice, but since it was decided that PA would be a suitable candidate for this research it did not matter. SLS can print bigger prototypes, but with the current test setup, bigger prints are not necessarily needed. Lastly, an earlier test print seen in Figure D.6 had been done with MJF. As seen in the picture, this print is of good quality. There are no test prints with SLS to compare the MJF test prints to. Therefore, it was decided that the final prototypes are to be created using MJF with a PA granulate.

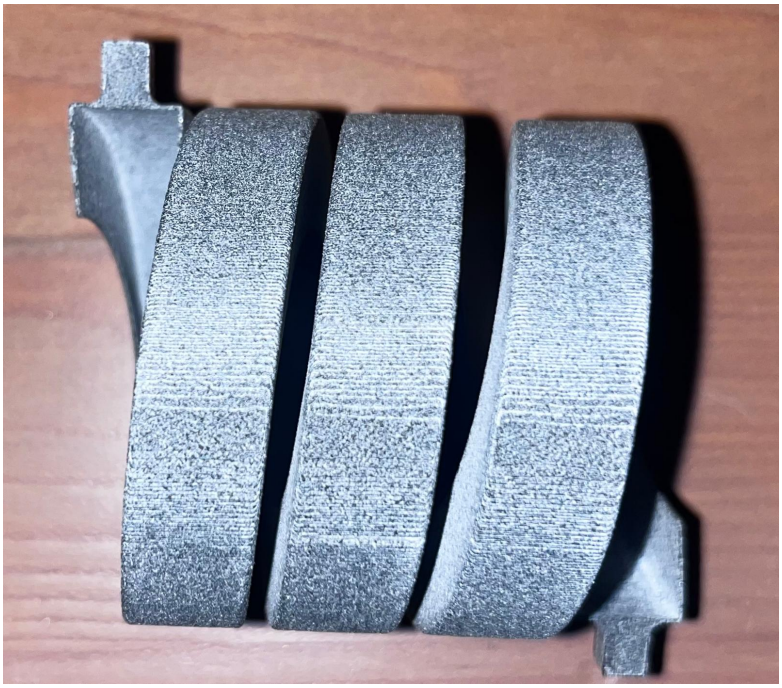

Figure D.6: Sample MJF print

E

Experimental accuracy testing

This appendix details extra experimental tests that are performed to further validate the accuracy of the tests presented in the report. This is needed, as a decrease in force magnitude is observed during consecutive tests on the same lattice. It is hypothesized that this decrease is caused by the visco-elastic storage of energy within the material, as it was noted that the measured load before testing decreased as well. To prove this two conditions would have to be met: The force-displacement curves should be consistent when tested for already explored deformation levels and no plastic deformation should have occurred.

To test the first condition of consistent force-displacement curves the lattices are tested in reverse order after the initial tests. In other words, the last compression step is repeated one time and from there decremental steps of 15 mm were taken. For the [7 x 6] lattice this meant covering a range from 90-0 mm in steps of -15 mm, resulting in Figure E.1. For the [14 x 10] lattice this meant covering a range from 135-0 mm in steps of -15 mm, resulting in Figure E.2. For reference, the *"Simulation - Fitted"* curves are identical to the curves in section 3.2. When looking at the figures it is observed the different force-displacement curves now lie neatly atop each other. This proves the curves are consistent when tracing earlier traced deformations.

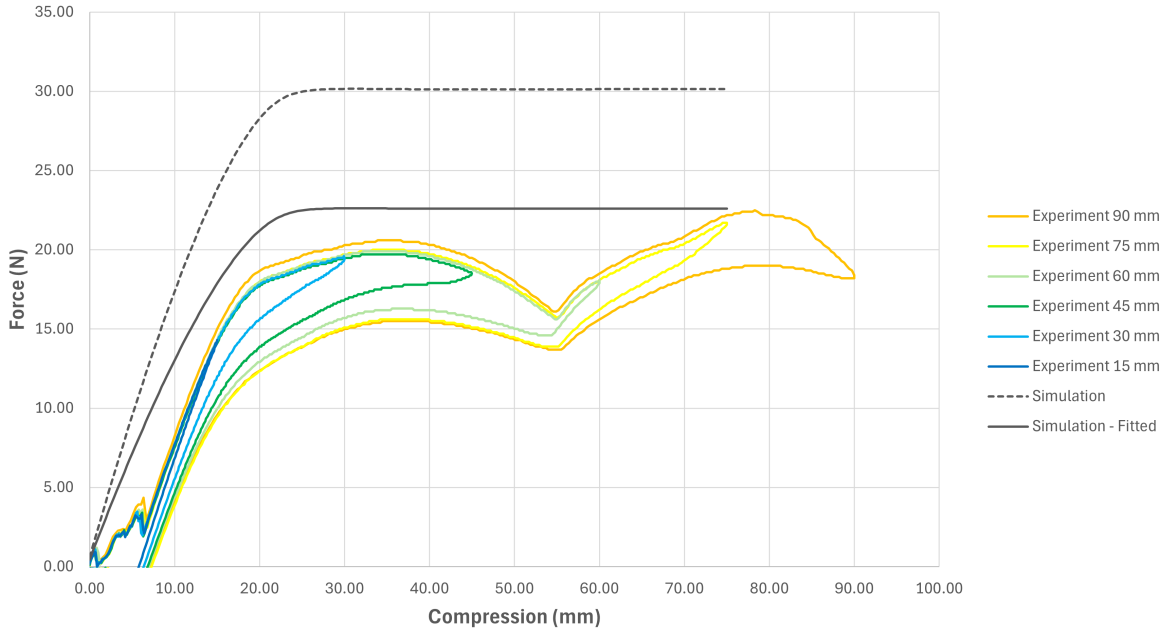

Figure E.1: Force-displacement [7 x 6] lattice experiment | Reverse order

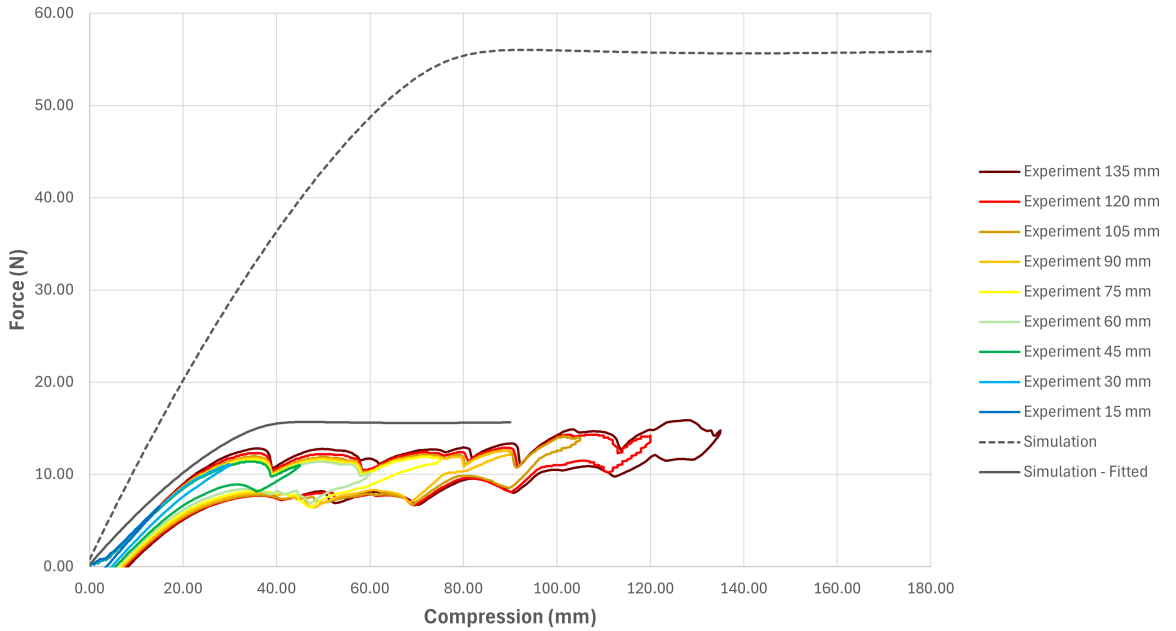

Figure E.2: Force-displacement [14 x 10] lattice experiment | Reverse order

To test the second condition that not plastic deformation occurred, the [14 x 10] lattice had another test performed on it 1 week after the original testing date. If no plastic deformation would have occurred, this would have been a sufficient time gap for the last visco-elastic energy to be dissipated. The [14 x 10] lattice was chosen as this lattice has been compressed the most, and therefore would have the highest change to enter a region of plastic deformation during testing. In Figure E.3 the 45 mm deformation curves of the original test, the reverse order test, and the test 1 week later are presented. For reference, the *"Simulation - Fitted"* curves are identical to the curves in section 3.2. When looking at the figure, the 1 week test curve fitted neatly atop the original test. If plastic deformation would have occurred, the 1 week test curve would lie closer to the reserve curve. Therefore, the decrease in force magnitude can be explained by the visco-elastic energy storage of the prototype.

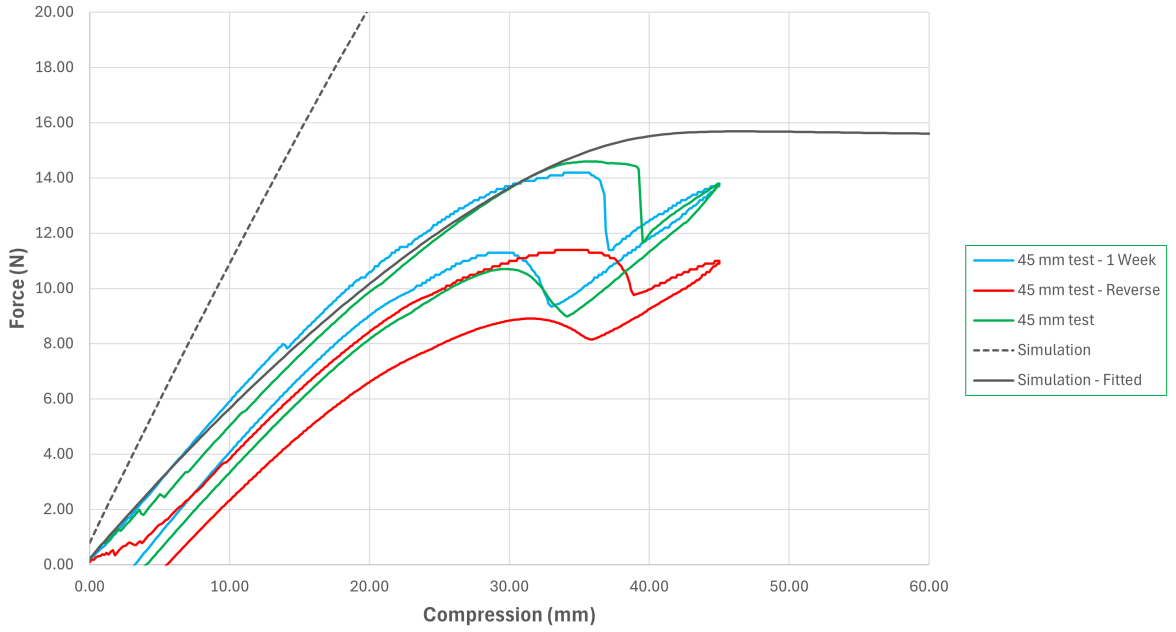

Figure E.3: Force-displacement [14 x 10] lattice experiment | Plastic deformation